

1 **Multitemporal UAV LiDAR detects seasonal heave and**
2 **subsidence on palsas**

3 Cas Renette¹, Mats Olvmo¹, Sofia Thorsson¹, Björn Holmer¹, Heather Reese¹

4 ¹Department of Earth Sciences, University of Gothenburg, Gothenburg, Sweden

5 *Correspondence to:* Cas Renette (cas.renette@gvc.gu.se)

6

7 **Abstract**

8 In the context of the accelerating impacts of climate change on permafrost landscapes, we use [an](#) uncrewed
9 aerial vehicle (UAV) [carrying a](#) LiDAR [scanner technology](#) to investigate seasonal terrain changes in palsas
10 – mounds of frozen peat – since other remote sensing methods have struggled to capture the full dynamics
11 of these landforms. We investigated two palsas (4–5 m in height) in Sweden's largest palsa mire complex,
12 where we performed five field campaigns between September 2022 and September 2023 to track intra-
13 annual frost heave and thaw subsidence. Our approach allowed us to create digital terrain models (DTMs)
14 from high density point clouds (>1,000 points/m²) and analyze elevation changes over time. We found that
15 both palsas heaved on average 0.15 m (and up to 0.30 m) from September to April and subsided back to
16 their height from the previous year, or slightly below, over the course of the following summer. At one of the
17 palsas, we observed [a](#) notable lateral degradation [hotspot](#) over the study period in a ~~300-225~~ m² area, with
18 0.5–~~2.0~~[1.9](#) m height loss, likely initiated during the preceding warm and wet summer months. Part of this
19 degradation occurred between September 2022 and April 2023, suggesting that the degradation of these
20 palsas is not limited to the summer months. Our study shows the substantial value of using UAV LiDAR for
21 understanding how permafrost areas are changing. It ~~helps facilitates in~~ tracking the ongoing effects of
22 climate change and highlights palsa dynamics that would not be captured by annual measurements alone.

23

24 1 Introduction

25 In the face of accelerating climate change, permafrost – defined as ground that remains at or below 0 °C
26 for at least two consecutive years (Harris et al., 1988) – is warming at a global scale (Biskaborn et al.,
27 2019). Permafrost regions hold an approximately 50% (1300±200 Pg) of the world's terrestrial carbon,
28 making them vital to the global climate system (Hugelius et al., 2020). A significant amount (415±150 Pg
29 carbon) is stored in northern peatlands, nearly half of which is affected by permafrost (Hugelius et al., 2020).
30 In the discontinuous and sporadic permafrost zones, peatland permafrost can be found in palsa mires,
31 consisting of peat plateaus and palsas. Palsas are peat mounds with a core of perennially frozen soil
32 (Seppälä, 1986). Palsa mires are a sensitive and heterogeneous ecosystem, which are vulnerable to
33 increased air temperatures and precipitation in the Arctic (Luoto, Fronzek, et al., 2004a).
34 ~~(Seppälä, 1986)P(Luoto, Fronzek, et al., 2004)~~In the face of accelerating climate change, permafrost –
35 defined as ground that remains at or below 0 °C for at least two consecutive years (Harris et al., 1988) – is
36 warming at a global scale (Biskaborn et al., 2019). The thickness of the active layer, which is the top layer
37 that thaws and freezes each year (Romanovsky & Osterkamp, 1995), is also increasing at many polar sites
38 (Smith et al., 2022). Palsas, which are peat mounds with a core of perennially frozen soil, are indicative of
39 permafrost presence and serve as particularly vulnerable indicators of climatic changes. They are generally
40 found in subarctic wetlands (Seppälä, 1986), in the discontinuous or sporadic permafrost zone. The climatic
41 space for palsas, typically with a mean annual air temperature between -3 °C and -5 °C and mean annual
42 precipitation <450 mm, according to Luoto et al. (2004a), is projected to disappear in Fennoscandia by the
43 end of the 21st century (Fewster et al., 2022). (Fewster et al., 2022; Leppiniemi et al., 2023). In recent
44 studies, an increasing lateral degradation rate of palsas is reported (Borge et al., 2017; Mamet et al., 2017;
45 Olvmo et al., 2020) which may have far-reaching consequences for these ecosystems and biodiversity of
46 the subarctic region (Luoto, Heikkinen, et al., 2004b; Swindles et al., 2015). For example, the loss of palsas
47 can lead to the decline of specialized plant species that are adapted to the unique, dry conditions of palsas.
48 Additionally, animals that depend on these habitats, such as certain bird species and small mammals are
49 affected (Luoto, Heikkinen, et al., 2004) (Luoto et al., 2004b). In addition to the threat to biodiversity, the
50 degradation of palsas also impacts reindeer herding, berry picking and transport for local communities, as

51 [these elevated, often dry, parts of the landscape shrink and become more fragmented. The transition from](#)
52 [a palsa to a lower lying, wet fen, is also associated with an increase in CH₄ and CO₂ emissions \(e.g.](#)
53 [Łakomiec et al., 2021; Pirk et al., 2024; Swindles et al., 2015; Voigt et al., 2019\) as the stored carbon in](#)
54 [these peatlands is subject to microbial re-mobilization when permafrost thaws. The climatic feedback](#)
55 [mechanism further highlights the need for continued monitoring of these environments. Therefore, palsa](#)
56 [mires are a priority habitat of the EU Species and Habitat Directive \(*EUNIS -Factsheet for Palsa Mires,*](#)
57 [2013\). However, in Sweden only about half \(47%\) of the total palsa area is situated within ~~some kind of a~~](#)
58 [protected area \(Backe, 2014\).](#)

59 ~~The degradation of palsas leads to significant changes in this landscape and ecosystem. In recent studies,~~
60 ~~an increasing lateral degradation rate of palsas is reported (Borge et al., 2017; Mamet et al., 2017; Olvmo~~
61 ~~et al., 2020), which may have far-reaching consequences for the biodiversity of the subarctic (Luoto, et al.,~~
62 ~~2004b; Swindles et al., 2015). The transition from an elevated, often dry, palsa bog to a lower lying, wet~~
63 ~~fen, is associated with an increase in CH₄ and CO₂ emissions (e.g. Lakomiec et al., 2021; Pirk et al., 2024;~~
64 ~~Swindles et al., 2015; Voigt et al., 2019). Due to the tendency to enhance atmospheric greenhouse gas~~
65 ~~emissions, degrading palsas therefore not only indicate but can also contribute to climatic change. This~~
66 ~~climatic feedback mechanism further highlights the need for continued monitoring of these environments.~~
67 ~~Therefore, palsa mires are a priority habitat of the EU Species and Habitat Directive (*EUNIS Factsheet for*~~
68 ~~*Palsa Mires*, 2013). However, in Sweden only about half (47%) of the total palsa area is situated within~~
69 ~~some kind of protected area (Baacke, 2014).~~

70 The degradation of permafrost in palsas is ~~Permafrost degradation of palsas is~~ indicated by both lateral
71 erosion and vertical subsidence. Lateral erosion refers to the horizontal shrinkage of the permafrost body
72 along the edges of palsas, often resulting in the formation or expansion of connected water bodies, i.e.,
73 thermokarst lakes (Martin et al., 2021). Vertical subsidence, on the other hand, involves the downward
74 sinking of the ground surface as a result of the melting of excess ground ice, leading to a drop in surface
75 elevation. In addition to this, the elevation of permafrost terrain fluctuates cyclically due to annual freeze-
76 thaw cycles within the active layer (Gruber, 2020; Iwahana et al., 2021), although this has not been explicitly
77 studied on palsas. During fall, freezing of water in the soil and its expansion, in addition to the formation of
78 seasonally segregated ice, can cause heaving of the terrain, while terrain subsidence, caused by the
79 melting of both pore ice and segregated ice, occurs during spring and summer (Fu et al., 2022). The melting
80 of excess ground ice (i.e., ice that is in excess of the total pore volume of the ground in unfrozen conditions;
81 Harris et al., 1988) below the active layer causes longer-term subsidence as result of permafrost thaw.
82 Therefore, thaw-subsidence rates are generally higher in ice-rich than in ice-poor permafrost soils (Gruber,
83 2020; Zwieback & Meyer, 2021).

84 While there is growing awareness of the importance of monitoring palsa mires, there is a lack of quantitative
85 measurements of their intra-annual heave and subsidence patterns. de la Barreda-Bautista et al. (2022)

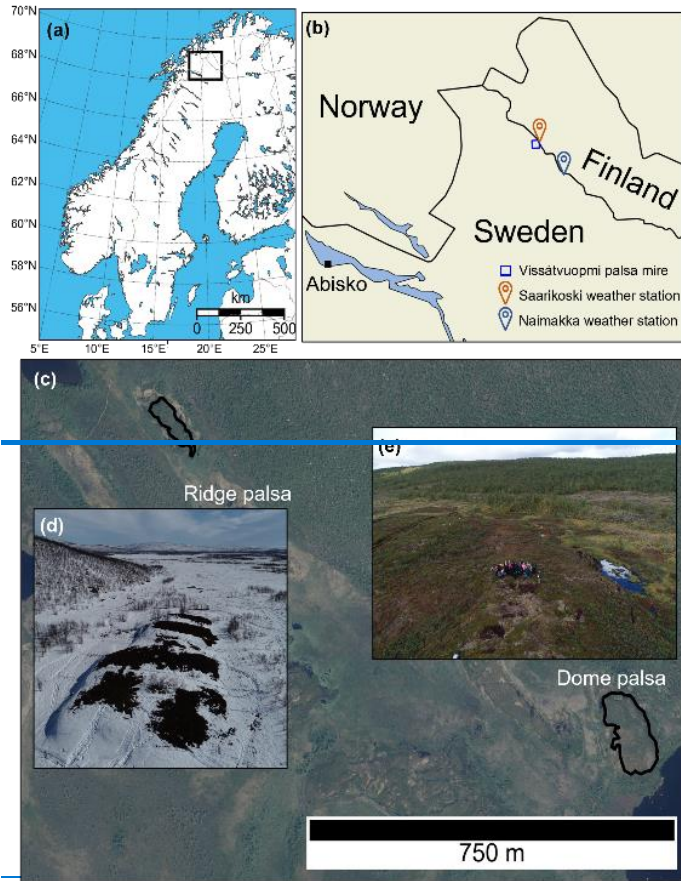
86 used InSAR data to analyze thaw-season subsidence on palsas in northern Sweden, ~~but findings~~ only
87 sub-cm scale surface level changes. They suggest that this method likely highly underestimated actual
88 displacement rates as a result of spatial averaging. In other recent studies with attempts to quantify both
89 lateral and vertical changes in palsas or peat plateaus, the focus was on multi-year timescales (e.g., Martin
90 et al., 2021; Verdonen et al., 2023) and not on changes occurring within a year. UAV photogrammetry to
91 create digital surface models (DSMs) to study palsas and peat plateaus has been applied more frequently
92 in recent years (e.g., de la Barrera-Bautista et al., 2022; Krutskikh et al., 2023; Martin et al., 2021; Verdonen
93 et al., 2023). However, as described in Verdonen [et al.](#) (2023), change analysis from DSMs created with
94 UAV photogrammetry is sensitive to relatively minor changes in vegetation and light conditions. Advances
95 in uncrewed aerial vehicles (UAV or drone) in combination with light detection and ranging (LiDAR)
96 technology (Ostrowski et al., 2017) have made it possible to collect accurate, high-resolution (cm-scale)
97 digital terrain models (DTMs) and DSMs. LiDAR sensors can prove advantageous over regular
98 photographic Red-Green-Blue (RGB) imagery, in that LiDAR can penetrate through small gaps in the
99 vegetation allowing creation of DTMs of the underlying ground, whereas ~~terrain elevation models from~~ RGB
100 cameras require clear sight to the ground surface. LiDAR can also be used in low-light conditions as
101 opposed to RGB imagery, which can be beneficial in the Arctic, where daylight is limited during parts of the
102 year. Another advantage that UAV LiDAR data holds is the absence of need of ground control points (GCPs)
103 due to the potentially low bias of UAV LiDAR data positional errors. This advantage drastically saves time
104 and thus costs on repeated visits (Harder et al., 2020). Therefore, the use of repeat UAV LiDAR scanning
105 is a promising tool for accurate change detection (Curcio et al., 2022; Harder et al., 2020; Jacobs et al.,
106 2021; Lin et al., 2019), but has not yet been widely used to monitor permafrost features.

107 In this study, our objective is to detect and quantify the intra-annual vertical heave and subsidence of two
108 palsas using repeat measurements from UAV LiDAR data. ~~Our findings show seasonal dynamics of the
109 palsas and highlight the substantial potential of UAV LiDAR scanning to study permafrost-mediated
110 landscape changes.~~

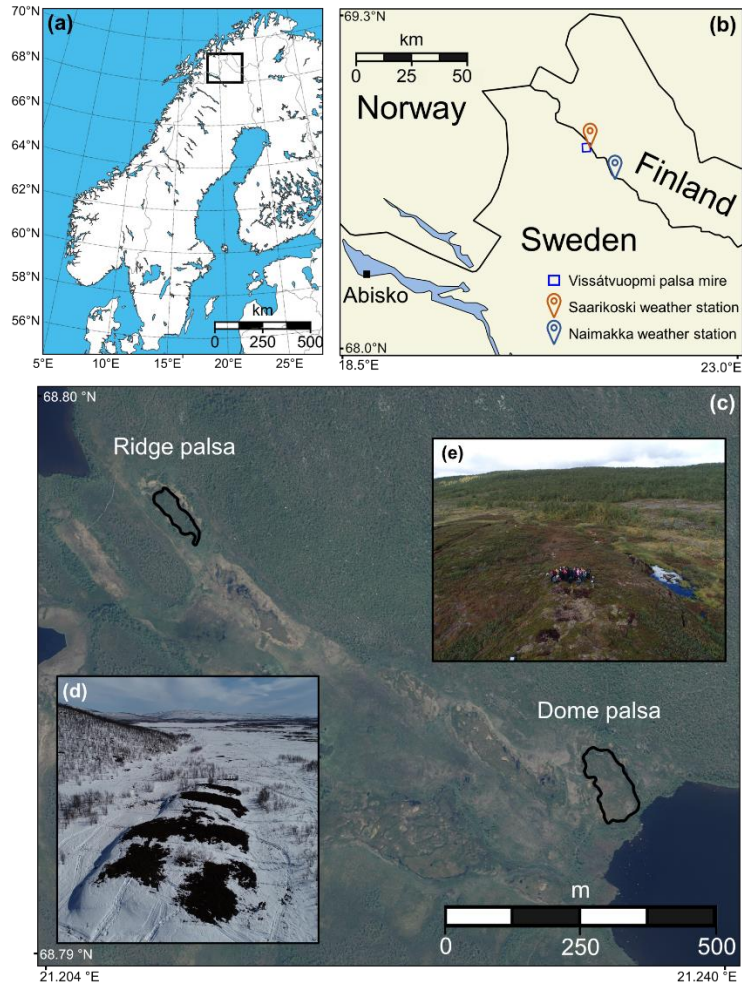
111 2 Study site: Vissátvuopmi palsa complex

112 Located near the Finnish border, and just southwest of the Kōnkämäeno river, Vissátvuopmi is the largest
113 [of the in total eight named](#) coherent palsa mire complexes in Sweden (ca. 150 ha of palsa area; Backe,
114 2014) at N 68°47'50", E 21°11'30" (Fig. 1). [According to InSAR data from 2017-~~to~~, 55% of the total area of](#)
115 [these eight palsa complexes is subsiding, compared to 98% of the Vissátvuopmi area \(Valman et al., 2024\).](#)
116 [Though notably, only Vissátvuopmi and Árbuvuopmi \(northwest of Vissátvuopmi\) are not part of the EU](#)
117 [Natura 2000 network.](#) ~~(Valman et al., 2024)~~

118 Surrounded by mountains up to 700 m a.s.l., the valley [in which Vissátvuopmi is located](#) has several larger
119 lakes, thermokarst features and fens. Two distinct palsas, one ridge-shaped and one dome-shaped (called
120 the "Ridge" and "Dome" palsas from hereon) situated at the foot-slope of a bedrock hill, are the focus of
121 this study and are located between 443 and 452 m a.s.l. (Fig. 1c). [Water tables typically do not rise above](#)
122 [the mire surface in most of the surroundings of the two studied palsas, except for thermokarst ponds that](#)
123 [border the palsas.](#) -In September ~~2022~~2023, the Dome palsa was approximately 170 meters in length and
124 75 meters in width, with [an area of 11408 m² and](#) its highest point about 4 meters above the surrounding
125 mire. The Ridge palsa measures about 125 meters in length and 40 meters in width, [with an area of 3522](#)
126 [m² and with](#) its highest point being roughly 5 meters above the adjacent mire terrain. The Dome palsa is
127 taller on its northern and eastern sides, while it flattens out on the western and southern sides. An [all-terrain](#)
128 [vehicle \(ATV\) ATV](#)-track runs over the northeastern part of the palsa, which most certainly contributes to
129 amplified degradation of the underlying permafrost by collecting snow and water. The track is visible in
130 aerial photos from 1994 but is absent in the 1963 photos. A natural depression in the center part of the
131 palsa has the same effect and further fragments this palsa. The Ridge palsa is smaller in area but slightly
132 taller. This palsa consists of several crests of similar elevation with depressions in between. The
133 southeastern margin of this palsa is 'tail-shaped' and of lower elevation.



134



135

136 **Figure 1. (a,b) Location of the Vissátvuopmi palsa mire complex and used weather stations in Northern**
 137 **Sweden. (c) Orthophoto from 2021 (© Lantmäteriet, 2021) showing a segment of the palsa mire and the location**
 138 **of the two studied palsas. (d) Oblique UAV image highlighting the partly snow-covered Ridge palsa in April**
 139 **2023. (e) [Aerial-view Oblique UAV image](#) of the Dome palsa in September 2023.**

140 The vegetation over the palsa mire complex is characterized by a mosaic of marshes with grasses and
 141 sphagnum mosses, wet heaths with willow, and drier areas with subalpine shrub heath. Birch forest occurs
 142 primarily on the slopes surrounding the mire, however, birches are also growing within the palsa mire
 143 complex. The palsa vegetation consists of dry heath and mesic heath (Andersson et al., 1985) where the
 144 field layer is predominantly low-growing *Betula nana* (< 35 cm in mean height), *Empetrum nigrum* ssp
 145 *hermaphroditum* and *Rubus chamaemorus*. The bottom layer consists of lichens in higher and drier areas
 146 of the palsa, while sphagnum mosses are in lower-lying, wetter areas. At the edges of the palsa, particularly

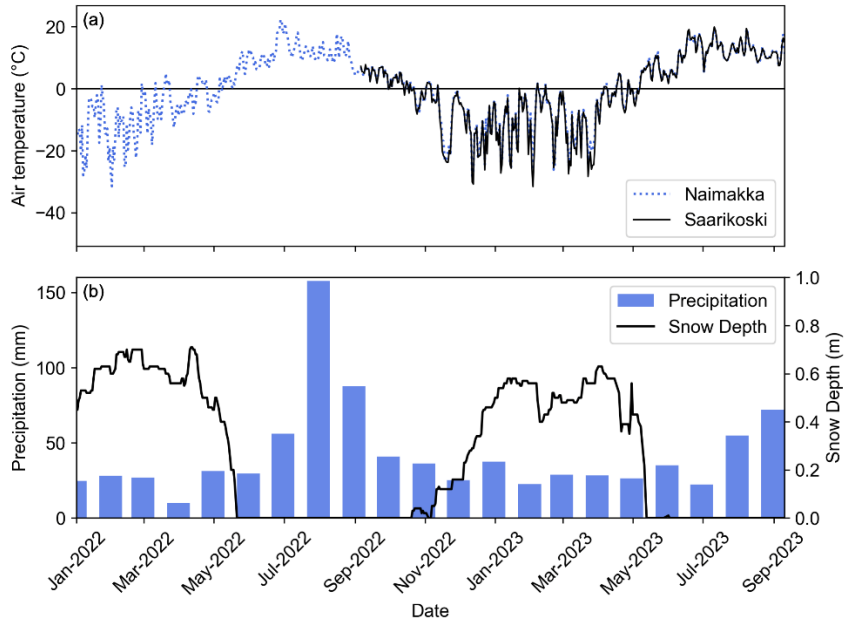
147 where pools of water have formed, grasses such as *Carex rotundata* and *C. saxatilis* are common, in
148 addition to *Eriophorum russeolum* (Backe, 2014). The ~~R~~idge palsa has a few birch trees growing on the
149 north and south parts of the palsa.

150 The Köppen climate type is Subarctic (Dfc) and a weather station operated by the Swedish Meteorological
151 Institute (SMHI) in Naimakka ([established in 1944](#)), ca. 18 km east of the study site observed a mean annual
152 air temperature of of -1.5 °C and mean annual precipitation was 460 mm in the 1991–2020 standard period.

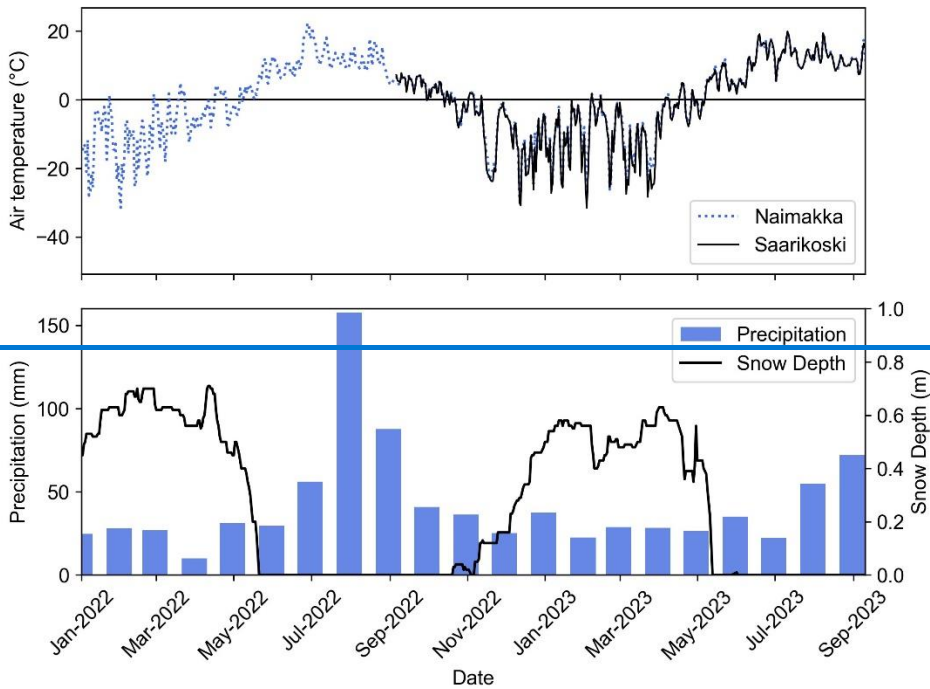
153 In September 2022, a ~~HOBO~~ [HOBO® U30-NRC \(Onset Computer Corporation\)](#) weather station was set
154 up in the nearby settlement of Saarikoski, ca. 1.5 km from the study site (see Fig. 1b for location of the two
155 weather stations). [At this station, air temperatures at 2 m above the ground surface are recorded at two-](#)

156 [hour intervals](#). Both precipitation and snow depth have been monitored [by SMHI](#) since 2015 at Saarikoski.

157 It is notable that in July 2022 the monthly precipitation was 158 mm, which is more than ~~aone-~~third of the
158 [normal](#) mean annual precipitation (Fig. 2).



159



160

161 **Figure 2. Weather data in the study region between January 2022 and September 2023. (a) Mean daily air**
 162 **temperature at ca. 1.5 km (Saarikoski) and at ca. 18 km (Naimakka) from the studied palsas. (b) Monthly**
 163 **precipitation and snow depth observed at Saarikoski.**

164 Based on aerial photo interpretation, Olvmo et al. (2020) reported average areal decay rates of $-0.71\%a^{-1}$
 165 and $-1.25\%a^{-1}$ in the Dome and Ridge palsa respectively between 1955 and 2016. Additionally, they

166 concluded that palsas in the Vissátvuopmi complex have most likely been in a phase of degradation since
167 the early 20th century.

168 3 Data and Methods

169 3.1 LiDAR data acquisition

170 We used repeat UAV-borne LiDAR scanning to obtain point clouds and create raster-based ~~digital terrain~~
171 ~~models~~ (DTMs) at a high temporal and spatial resolution. Flights were performed on 4 September 2022, 26
172 April 2023, 18 June 2023, 19 July 2023, and 7 September 2023. We conducted the scans on these dates
173 to capture the state of the palsas at the end of summer, then observed them when frozen, and continued
174 tracking them throughout the proceeding thawing season. A DJI Matrice 300 RTK UAV was equipped with
175 a YellowScan Mapper (YSM) LiDAR scanner in September 2022 and a YellowScan Mapper + (YSM+) in
176 all following flights (Fig. 3). These are lightweight Livox LiDAR scanners with an Applanix GNSS/INS
177 system. Table 1 shows the properties of the flights and scanner(s). The vertical accuracy and precision of
178 these specific LiDAR scanners are determined by the manufacturer. They performed 15 flight lines for
179 YSM+ and 13 for YSM at velocities between 5 and 10 m/s and between heights between 50 and 120 m.a.g.l.
180 over a series of surfaces. The assessment with 18 ground 18-truth points then resulted in the values given
181 in Table 1. All surveys in this study weare performed within one year of the calibration. For both ~~of the~~
182 palsas, a flight with high overlap was done and supported by a second flight with additional orthogonal
183 trajectories. The same flight plans were executed for all five scannings to ensure equal spatial coverage
184 and resolution.



185
 186 **Figure 3. DJI Matrice 300 RTK equipped with the YellowScan Mapper_+ in front of the Ridge pPalsa.**

187 The April 2023 flights were performed during a period of snowmelt, so that parts of both palsas were snow-
 188 free, while other parts remained snow-covered. Consequently, in order to investigate changes in terrain
 189 elevation, the snow-free parts needed to be isolated for analysis. For that reason, flights with a second UAV
 190 ([DJI Phantom 4 Pro v2.0](#)) with an RGB camera to create orthomosaics were performed on the same day
 191 as the LiDAR scanning.

192

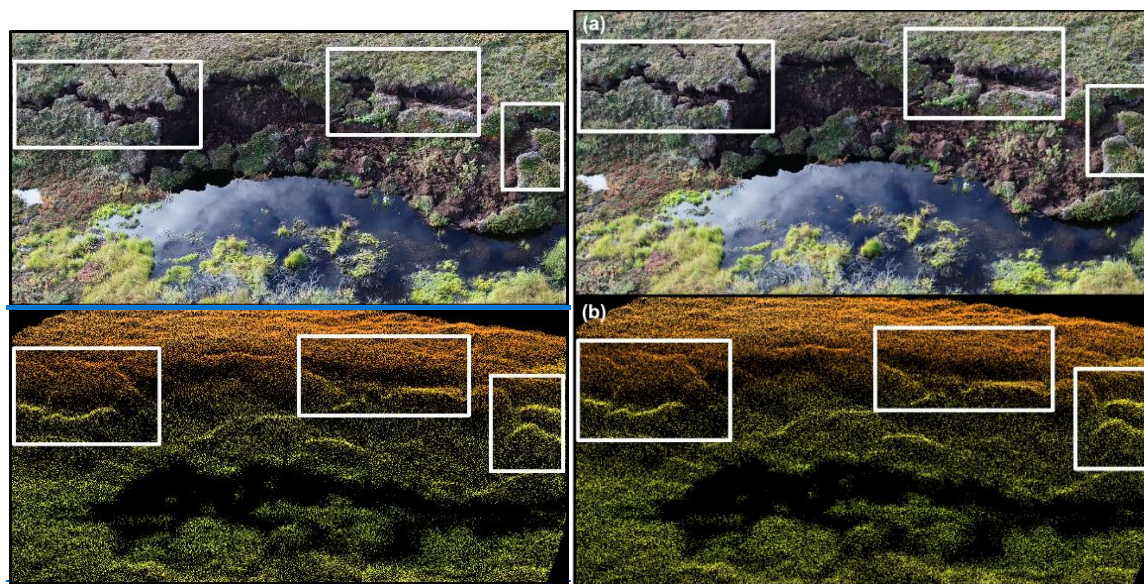
193 **Table 1. LiDAR scanner and flight parameters of the [flying-flight](#) missions. Where values for YellowScan**
 194 **Mapper differ from YellowScan Mapper_+, they are shown within parentheses.**

Parameter	Value, YellowScan Mapper_+ (Mapper)
Vertical Accuracy (RMSE, m)	0.021 (0.028)
Precision (m)	0.024 (0.032)
Number of returns	3 (2)
Altitude (m.a.g.l.)	60
Velocity (m/s)	8
Overlap (%)	60

195

196 Regarding the UAV LiDAR flights, the average flight time was 6 minutes and 49 seconds over the Dome
 197 palsa, and slightly shorter over the Ridge palsa at 5 minutes and 13 seconds. Similarly, flights over the
 198 Dome palsa yielded a slightly larger coverage area of 53993 m² compared to the Ridge palsa, which
 199 covered an area of 42072 m², including part of the surrounding mire and forested mountain. The mean

200 point densities over the Dome palsas were 1327 (YSM) and 1462 (YSM+) points/m², and 1201 (YSM) and
201 1519 (YSM+) points/m² at the Ridge palisa. These pulse densities can be regarded as very high, easily
202 allowing the creation of DTMs with high spatial resolution. Terrain features such as surface cracks and
203 blocks of peat are well-identifiable in the LiDAR point cloud data, which emphasizes the high quality of the
204 collected data (Fig. 4).



205
206 **Figure 4. (a) RGB photo of a degrading edge and formation of a thermokarst lake at the Dome palisa, taken with**
207 **a DJI Phantom 4 UAV in September 2022. (b) Dense UAV LiDAR point cloud taken on the same day with the**
208 **DJI Matrice 300 RTK equipped with the YellowScan Mapper. Morphological features such as cracks in the**
209 **surface and individual blocks of peat can clearly be recognized in the point cloud. This section of the palisa**
210 **reaches a height of ca. 4 meters.**

211 **3.2 Point cloud processing and DTM creation**

212 The processing of a LiDAR point cloud requires several steps, including GPS correction, strip adjustment,
213 classification of ground points, and the creation of a DTM raster. The position data captured by the LiDAR
214 system during the flights weare postprocessed in PosPac UAV v. 8.2 ([PosPac UAVApplanix](#), 2023) using
215 PP-RTX for trajectory correction. PP-RTX for UAV uses the Trimble CenterPoint® RTX™ correction
216 service, which computes corrections to satellite orbit and clock data for trajectory correction and positioning,
217 based on a global network of tracking stations. This cloud-based solution gives centimeter-level positioning

218 accuracy without the requirement to set up a local base, which makes PP-RTX particularly advantageous
219 for UAV surveys in remote regions. YellowScan's processing software, CloudStation
220 ([YellowScanCloudStation](#), 2023), ~~wais~~ then used for strip adjustment to reduce the relative adjustment
221 error. The point clouds were compared visually for alignment in areas where changes were least likely.
222 Following this, CloudCompare v. 2.12.4 ([CloudCompare, 2023](#)~~(GPL software, 2023)~~) ~~wais~~ used to perform
223 the classification of points into ground and non-ground points using the Cloth Simulation Filter (CSF) (~~W.~~
224 Zhang et al., 2016). The CSF method simulates a virtual cloth dropping onto the inverted point cloud. Points
225 that are close to where the cloth settles are classified as ground, while those that are farther away are
226 considered non-ground. The software allows three adjustable parameters for the CSF classification.
227 Several parameter combinations were tested and the best result, based on visual inspection of the resulting
228 point cloud, was achieved with the following parameters: 'Cloth resolution' = 0.10 m (matching the resolution
229 of the created DTMs), 'Max iterations' = 500 and 'Classification threshold' = 0.10 m (controlling the distance
230 of points to be classified as ground), resulting in a detailed ground surface. Only ground points ~~were~~
231 used to create the DTM, and in this project a grid cell resolution of 0.10 m was chosen. Since the total
232 thickness of the point cloud along the ground ~~wais~~ between ca. 0.10 and 0.30 m, the minimum elevation
233 per grid cell ~~wais~~ used during the rasterization in order to ensure that the raster represents the ground
234 elevation. [A comparison of the lowest point and the 25th percentile elevation in 100 random 0.10 m by 0.10](#)
235 [m areas on each palsa was carried out, which showed no outliers at the ground level.](#) -This process ~~wais~~
236 carried out for all five time points, creating a DTM for each scanning and palsa. Finally, the resulting DTMs
237 ~~were~~ used for change detection by subtracting values of one raster from another. [For the change](#)
238 [detection, the error range was calculated following the topographic error propagation law \(Taylor, 1997\),](#)
239 [where the propagated error was described as the root sum of squares \(RSS\) of individual errors. For the](#)
240 [individual errors, those described in Table 1 were used.](#)

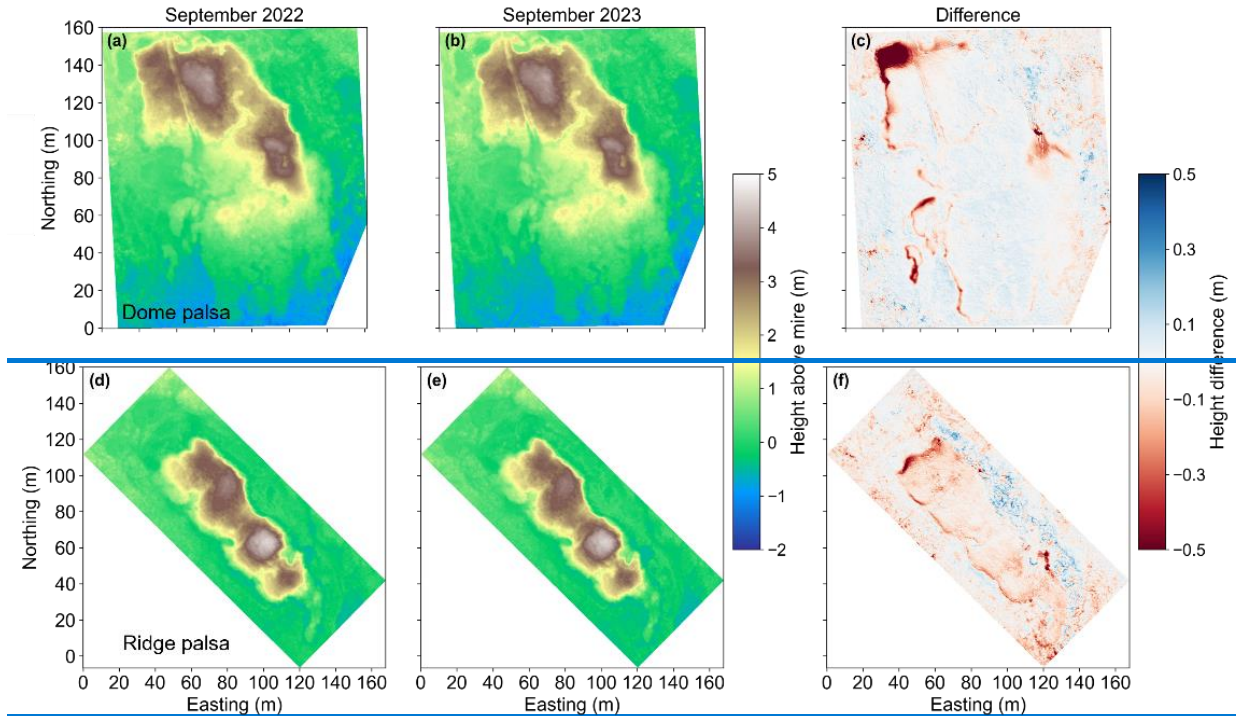
241 The snow free parts ~~of the palsas~~ from the April 2023 data were singled out for the computation of heave
242 and subsidence. ~~This-These areas were identified using~~~~was done with~~ georeferenced orthophotos taken
243 on the same day [in April](#) as the LiDAR data, in combination with a hillshade image from the DTM (since the
244 hillshade is smooth where there is snow). [Orthophotos that were taken on the same day as the LiDAR](#)
245 [surveys in September 2022 and September 2023](#) ~~awere~~ used to determine the extent of the palsas. For

246 each DTM, the mean elevation of the palsa's surrounding mire-wais computed and subtracted from the
247 DTM, which normalizes the elevation of the palsa into the height above the miresurroundings. Since the
248 definition of palsas is morphological (Harris et al., 1988), the height above its surroundings is per definition
249 the height of the palsa. For the normalization, we used the previously mentioned orthophotos to create a
250 polygon around each palsa, for which the mean elevation ~~was~~ taken per LiDAR flight. Areas ~~that~~containing
251 open water at any of the time steps, either thermokarst lakes directly around the palsas or other ponds,
252 are not included in these polygons. ~~The~~ simplifies transformation from elevation to height, simplifies
253 the comparison between the data from the different flights. Since the mire in April was snow-covered, the
254 mire elevation from the closest date (June) was taken for normalizing the April DTM.

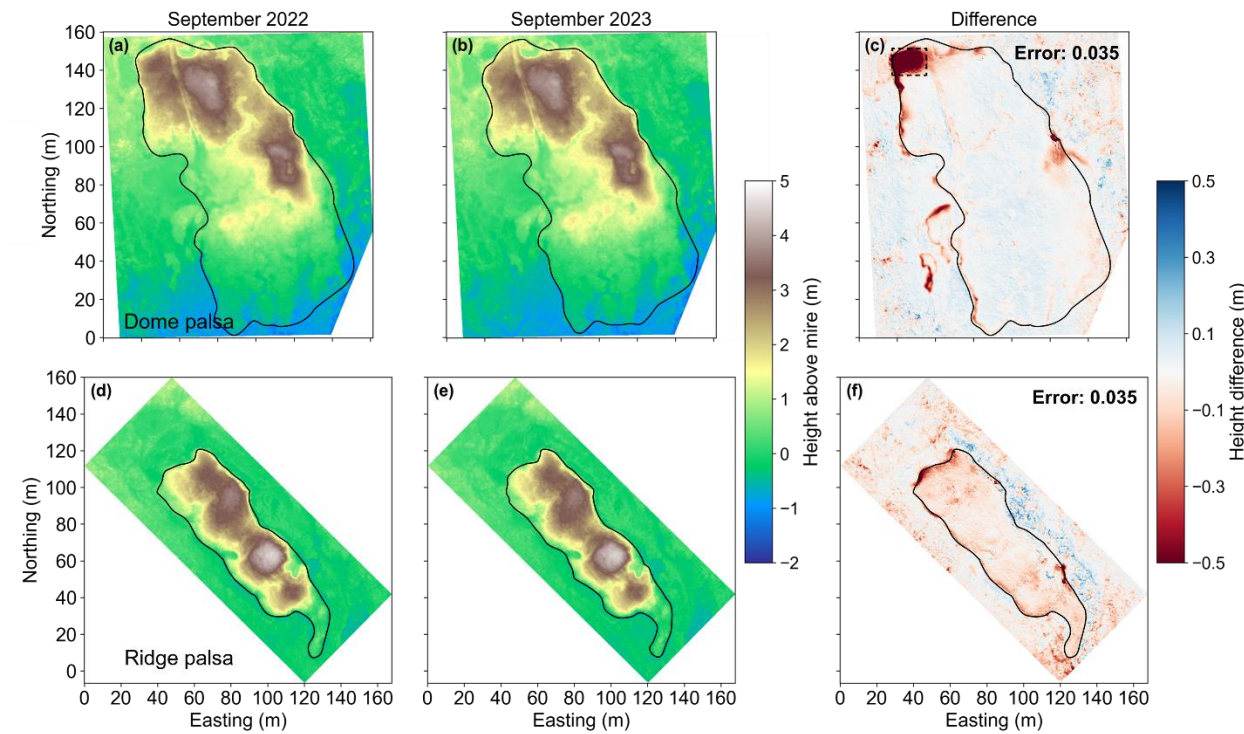
255 4 Results

256 4.1 Annual terrain changes from UAV LiDAR

257 Between September 2022 and September 2023, both palsas underwent degradation along their margins
258 (Fig. 5). ~~The largest height change was observed along the northwest edge of the Dome palsa, where an~~
259 area of 225 m² (2.6% of the total palsa area) subsided up to 1.9 m and on average 0.85 m. This corresponds
260 to a 34% height loss on this part of the palsa ~~in. the maximum height difference was 0.03 m, (from 4.21 m~~
261 to 4.18 m) on the Dome palsa and 0.05 m (4.67 m to 4.62 m) on Ridge palsa (Fig. 5). ~~From hereon we~~
262 name this ~~part~~300225 m² area the 'degradation hotspot'. ~~wawa (Table 1)we~~The largest change in height
263 was detected along the northwest edge of the Dome palsa where an area of ca. 300 m² subsided between
264 from 0.5 and 2.0 m. Degradation also occurred ~~also occurred~~ along the margins of the Dome palsa, as well
265 as within the ATV track that borders the eastern side of this ~~the new 300 m² degraded area~~degradation
266 hotspot. The height of the Ridge palsa decreased slightly over the entire landform, with most loss along the
267 margins in the form of lateral degradation.



268



269

270 **Figure 5. DTMs of the Dome (a,b,c) and Ridge (d,e,f) palsas on UAV LiDAR scans in September 2022 and**
 271 **September 2023. The black lines represent the extent of the palsas, based on orthomosaics from the same day**
 272 **as the UAV LiDAR surveys. The images-difference maps (c,f) highlight show the topographical changes over**

273 one year, with the palsa extent from the September 2022 flights orthomosaics in black. The dashed box in (c)
274 shows the 'degradation hotspot' on the Dome palsa.

275 4.2 Seasonal terrain changes from UAV LiDAR

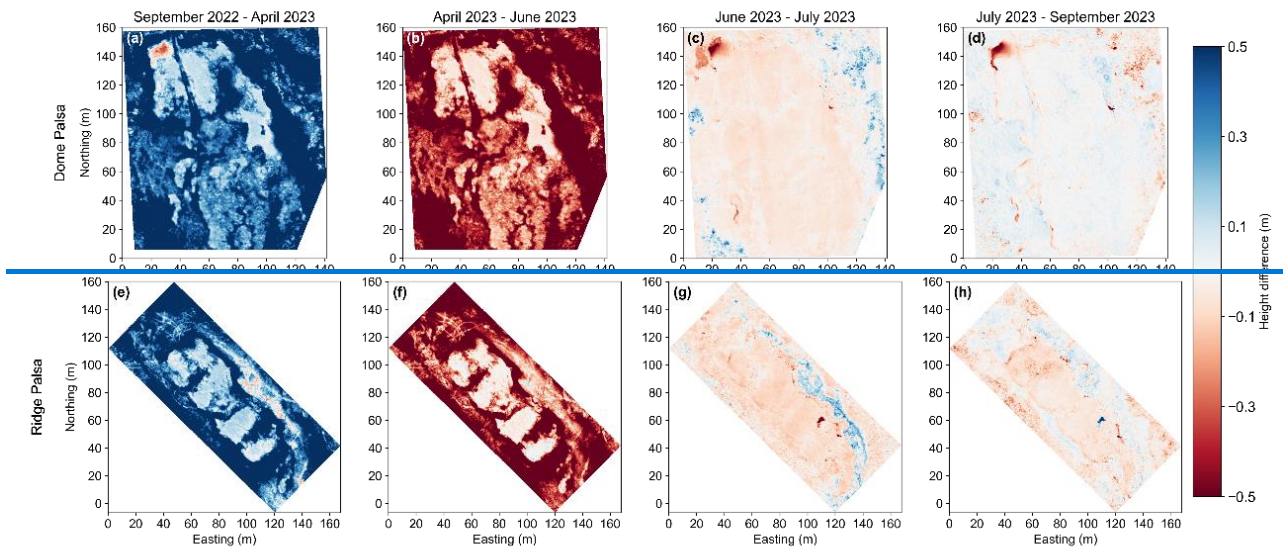
276 By comparing ~~each~~ DTMs ~~from consecutive with the following periods~~, we observed intra-annual terrain
277 variations, i.e., frost heave and thaw subsidence ~~on the two studied palsas~~. Change maps for the different
278 time steps are shown in Figs. 6a–h, while Figs. 6i–p are corresponding histograms of change. The first
279 two time steps are largely affected by snow cover in April, hence the histograms of change show both the
280 entire palsa as well as only the snow-free parts (Figs. 6i–p).

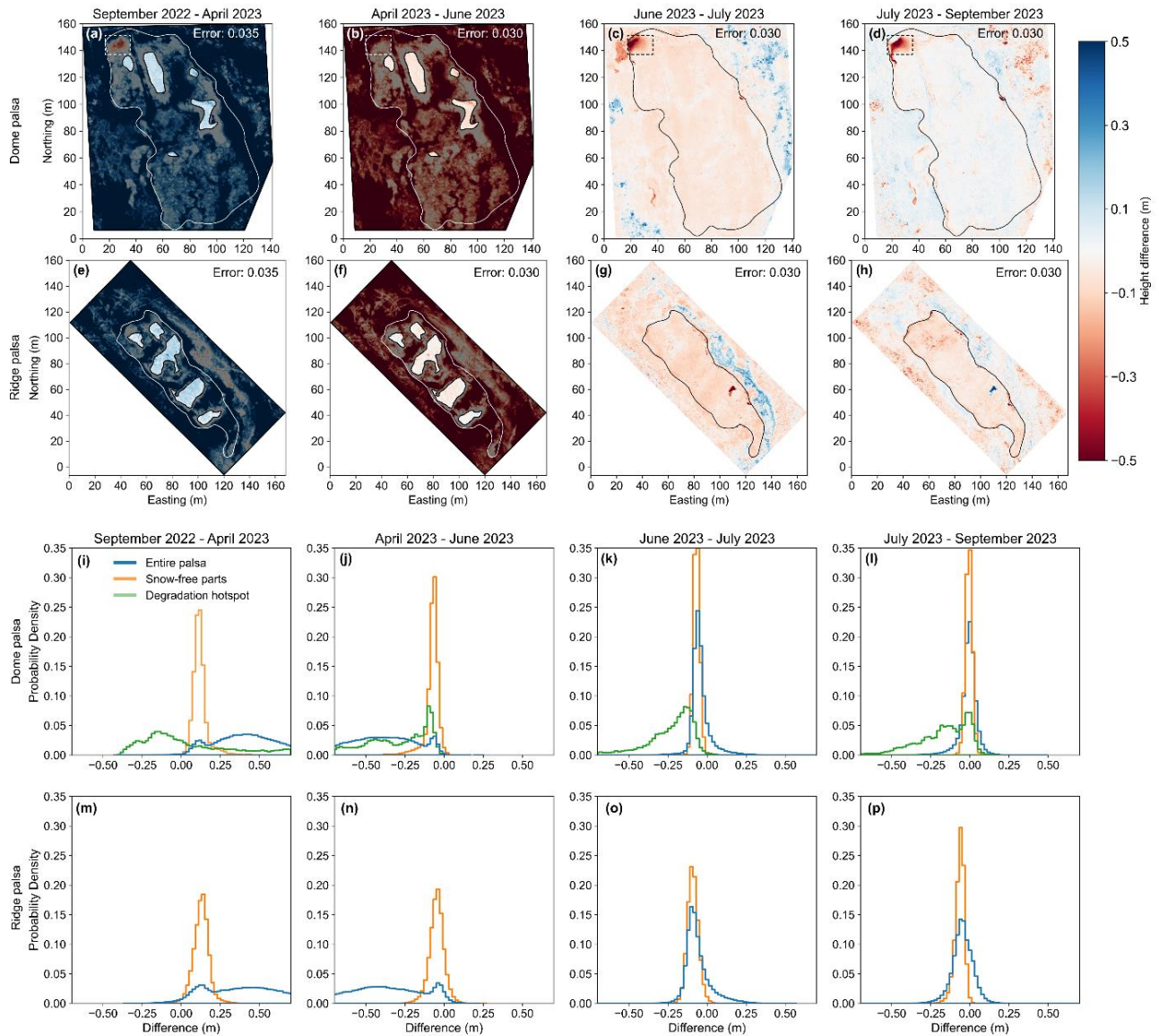
281 ~~(Fig. 6). April to June change histograms as well~~ The heterogeneous snow cover that affects this pattern
282 is more clearly visible in Fig. 7c and d. The snow thickness is up to ca. 2.0 m at the eastern margin of both
283 palsas and 1.0 to 1.5 m in the depressions, while the crests remain snow-free (also see Fig. 1d).

284 ~~Most interestingly, on these~~ snow-free crests ~~there was~~ (i.e. Fig. 7f), an elevation increase (heave) of up
285 to 0.30 m and on average of 0.15 m from September 2022 to April 2023 ~~for both palsas (Figs. 6aX and 6e)~~
286 ~~X) is observed.~~ ~~Comparing these two closeup parts of the Ridge palsa profile also shows that the~~
287 ~~subsidence the palsa underwent throughout the year in the depressions was larger than on the crests.~~

288 Between June and July, both palsas clearly subside ~~all over~~ the whole area (Figs. 6c and 6g), on average
289 0.05 m on the Dome palsa and 0.08 m on the Ridge palsa. Subsidence from July to September is only clear
290 on the Ridge palsa, with 0.05 m on average over the entire palsa ~~(Fig. 6hX)~~. ~~Despite being snow-covered~~
291 ~~in April, the degradation hotspot in the northwestern part of the Dome Palsa displayed a heightn-elevation~~
292 ~~difference~~ decrease of up to 0.4 m between September 2022 and April 2023 (Fig. 6a and 6–i), indicating
293 that subsidence in this area occurred between these months.

294 ~~Comparing these two closeup parts of the Ridge palsa profile also shows that the subsidence the palsa~~
295 ~~underwent throughout the year in the depressions was larger than on the crests.~~





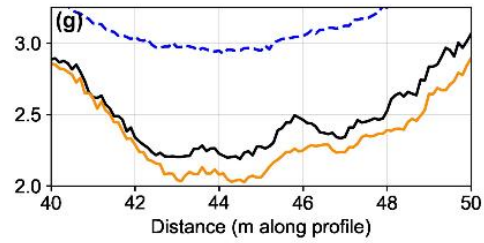
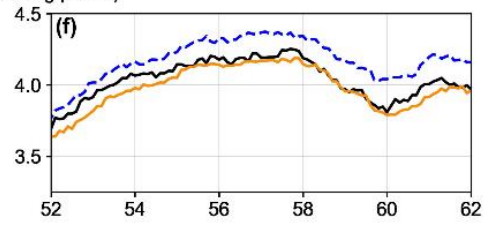
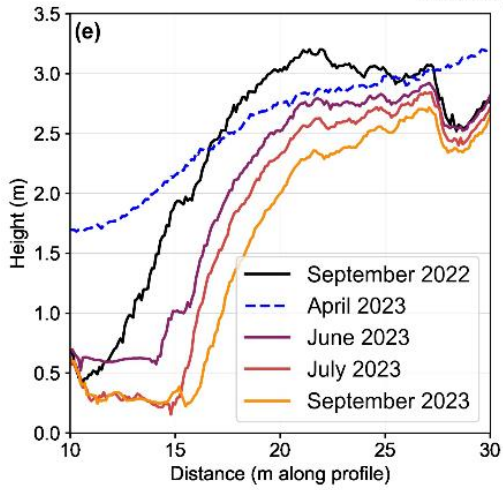
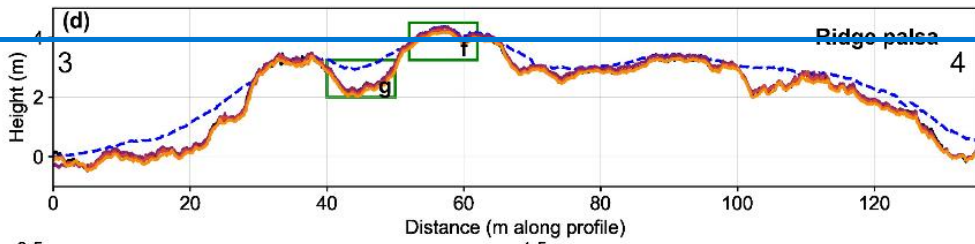
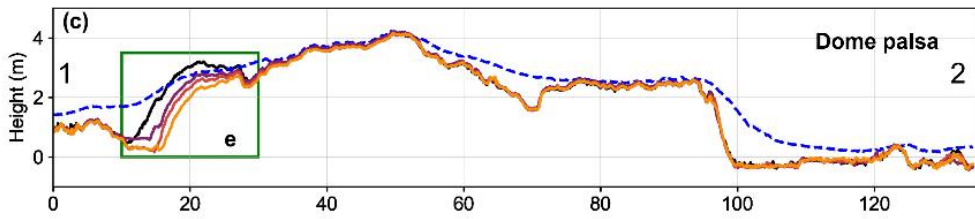
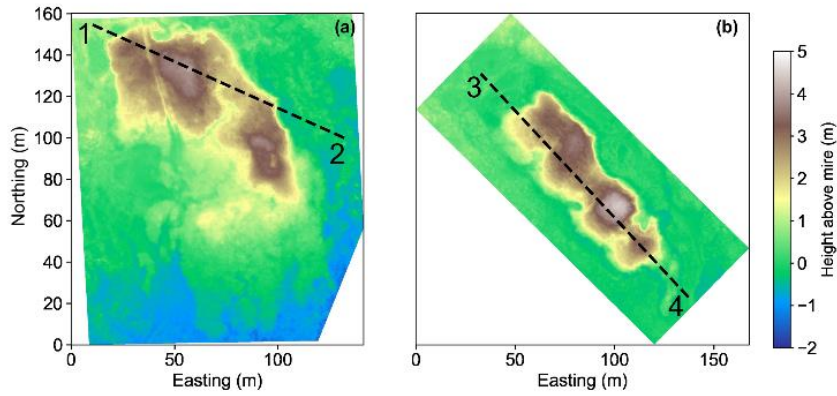
297

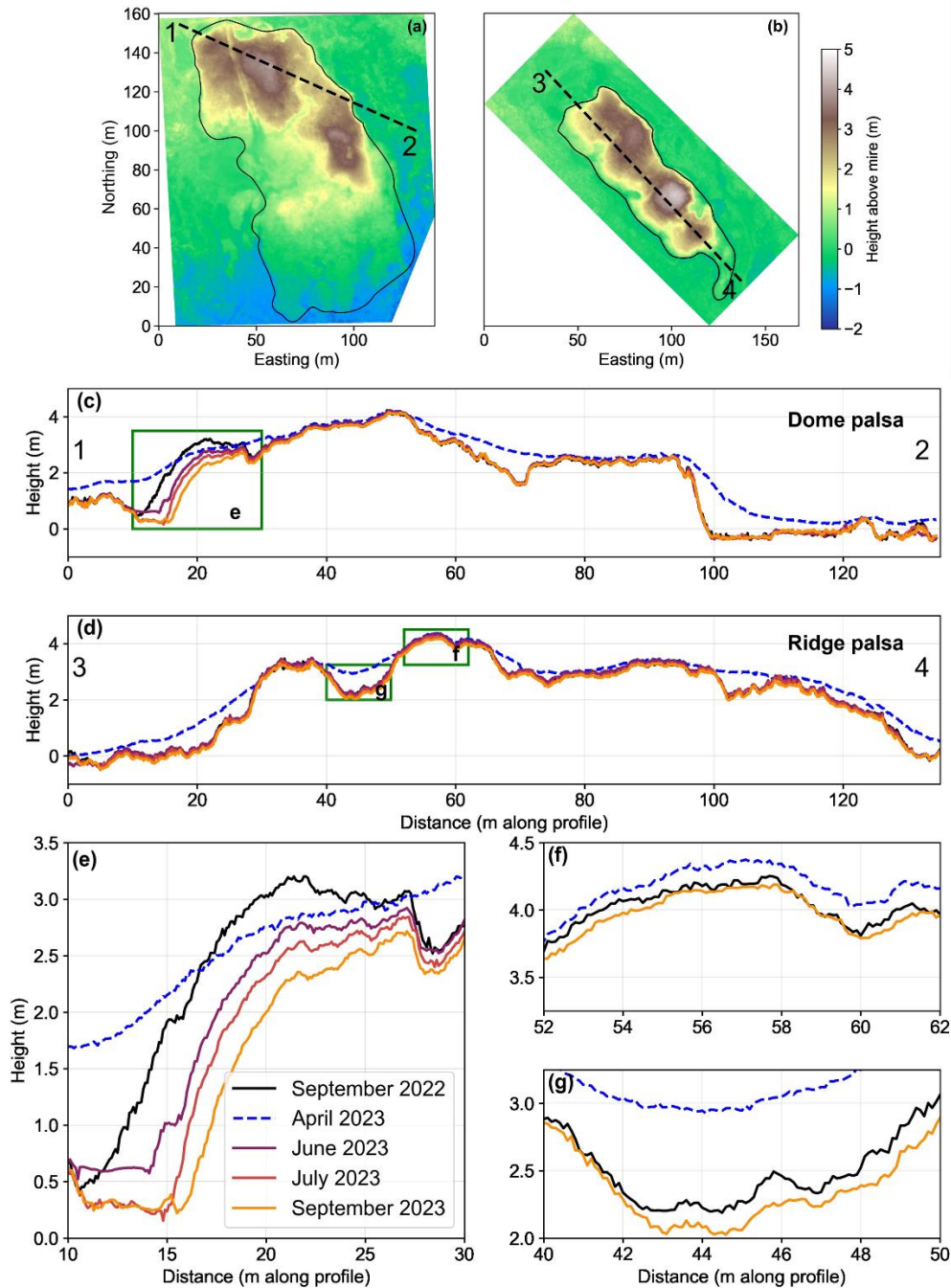
298 **Figure 6. Sequential height difference maps of the Dome (a,b,c,d, with the ‘degradation hotspot’ in the dashed**
 299 **rectangles) and Ridge (e,f,g,h) palsas between each-of the five UAV LiDAR DTMs from September 2022 to**
 300 **September 2023. Each panel showcases the topographical changes over successive intervals. Blue colors**
 301 **indicate elevation gains and red colors indicate elevation losses. The areas that were snow-covered areas (a,**
 302 **b, e, f) are greyed out, leaving the snow-free parts highlighted. The snow cover in April is mostly responsible**
 303 **for changes observed to and from those panels. Panels i–p display histograms with the distribution of height**
 304 **changes, separated into the entire palsa area (including snow-free parts), snow-free parts only, and the**
 305 **‘degradation hotspot’ on the(Dome palsa only), showing the distribution of changes over these areas.**

306

307 ~~Even despite the snow cover in April, the degradation hotspot in the northwestern part corner of the Dome~~
308 ~~Palsa shows signs of degradation subsidence up to 0.4 m (Fig. 6a, i), indicating it occurred sometime~~
309 ~~between September 2022 and April 2023. Figure 7 shows a time series of elevation changes along profiles,~~
310 ~~providing another way to look at the heave and subsidence. The is degradation hotspot is seen in Figs. 7c~~
311 ~~and 7e, remains evident and increases throughout the time series and is visible in Fig. 7c and e, where this~~
312 ~~area progressively degraded vertically up to 1.9 2.0 m between September 2022 and September 2023. The~~
313 ~~ATV track that crosses the Dome palsa shows a subsidence of 0.2–0.3 m just over the time period in this~~
314 ~~study (at ca. 27–29 m in Fig. 7e). On the Ridge palsa it can be seen in Figs. 7f and g that the subsidence~~
315 ~~was greater in the depressions than on the crests. The heterogeneous snow cover is visible in Figs. 7c~~
316 ~~and d. The snow thickness is up to ca. 2.0 m at the eastern margin of both palsas and 1.0 to 1.5 m in the~~
317 ~~depressions, while the crests remain snow-free (also see Fig. 1d).~~

318 ~~This degradation remains evident and increases throughout the time series and is visible in Fig. 7c and e,~~
319 ~~where this area progressively degraded vertically up to 2.0 m between September 2022 and September~~
320 ~~2023. Additionally, the ATV track that crosses the Dome palsa shows a deepening subsidence of 0.2–0.3~~
321 ~~m just over the time period in this study (at ca. 27–29 m in Fig. 7e).~~

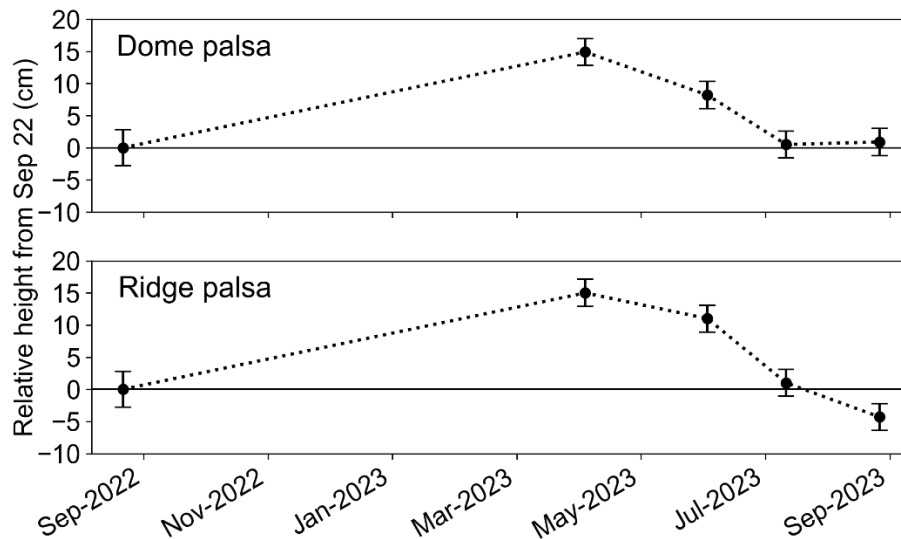
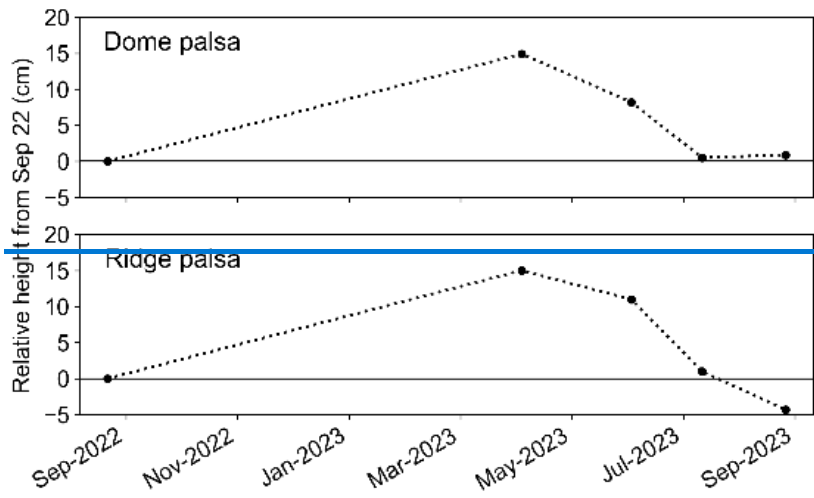




323

324 **Figure 7. Elevation profiles of the Dome and Ridge palsa based on UAV LiDAR DTMs from September 2022 to**
 325 **September 2023. (a,b) September 2022 DTMs with the according corresponding palsa outline. The dashed lines**
 326 **denote the location of the elevation profiles 1–2 and 3–4. (c) and (d) provide a general elevation overview of**
 327 **the transect, while (e), (f), and (g) offer zoomed-in views of specific areas of interest, indicated by the green**
 328 **boxes. The profile from April 2023 is mostly showing the snowpack, although some peaks are snow-free (see**
 329 **also Fig. 1d).**

330 The mean height of both palsas, calculated by taking all pixels within the snow-free areas, increased 0.15
 331 m between September 2022 and April 2023 (Fig. 8). The subsequent flights throughout the summer season
 332 show a successive lowering of the palsa height, i.e., subsidence. As shown in Fig. 6, the rate of subsidence
 333 is highest between the June and July flights. The ~~dome~~-Dome palsa returned to a similar mean height in
 334 September 2023 as compared to September 2022, while the snow-free parts on the ridge-Ridge palsa
 335 subsided to a 0.04 m lower mean height in September 2023 than in September 2022, which is also shown
 336 in Fig. 5. Overall, the heave and subsidence pattern is very similar across the two studied ~~ds~~ palsas.



337
 338
 339 **Figure 8. Heave and subsidence on the two studied palsas during the 2022-2023 year. Mean height changes**
 340 **relative to September 2022 are plotted (only for the areas that were completely snow-free in April 2023). The**

341 [cumulative changes of the intermediate steps add up to the total change from September 2022 to September](#)
342 [2023. The error bars represent the scanner specific RMSE for the respective LiDAR scanners used.](#)

343

344

345 5 Discussion

346 5.1 Intra-annual ~~terrain dynamics~~ heave and subsidence on palsas

347 The objective of this study was to elucidate and quantify the intra-annual dynamics of two large palsas in
348 the Vissátvuopmi palsa mire, and to achieve this, the use of UAV LiDAR proved to be an extremely suitable
349 tool. Analysis of the DTMs indicated that both palsas had frost heave of ca. 0.15 m on average between
350 September and April, and subsequent thaw subsidence from April to September. This is the first study that
351 covers these dynamics on palsas in such high spatial resolution, although seasonal terrain variability has
352 been investigated in other permafrost environments (Gruber, 2020; Hu et al., 2022; Iwahana et al., 2021;
353 Lin et al., 2019). For example, the heave and subsidence detected in this study are similar to values (0.10
354 – 0.14 m) observed in the GNSS positioning survey by (Iwahana et al., 2021) on an intact tundra site in
355 Alaska after the warm summer of 2019.

356 The largest rate of subsidence in our study occurred between June and July 2023, which was 0.07–05 m
357 on the Dome palsa and 0.40–08 m on the Ridge palsa. Freeze-thaw cycles within the active layer cause
358 frost heave and thaw subsidence, partially due to the density difference between water and ice. However,
359 the average observed heave of 0.15 m cannot be explained alone by this process and requires the formation
360 of seasonal segregation ice (i.e. ice lenses) within the active layer (Fu et al., 2022; Iwahana et al., 2021).
361 Alternatively, processes within the core of the palsa, for example, the infiltration and refreezing along
362 meltwater pathways, might result in seasonal heave and subsidence. To make more conclusive statements
363 about the exact mechanisms, it would be necessary to obtain complementary observations from the interior
364 of these palsas, in the form of soil and ice cores. Taking this step in the future would allow the observed
365 changes in the terrain morphology such as those done here to be better understood in relation to internal
366 palsa dynamics.

367 The 0.15 m heave is computed on the areas that were snow-free in April and are thus biased towards the
368 crests of the palsas that have a thinner active layer (see Appendix A) as they have a thinner winter snow
369 cover, which limits the insulation of the ground below. Since the magnitude of the heave and subsidence
370 depends on the thickness of the active layer (Iwahana et al., 2021), the areas with a deeper active layer

371 (i.e., those not included in the computation due to remaining snow in April) are therefore expected to have
372 undergone an even larger increase in height between September 2022 and April 2023. A process other
373 than freeze-thaw dynamics that could have affected the LiDAR measurements is the seasonal oscillation
374 of the peatland surface height due to water table fluctuations, called 'mire breathing' (Kellner & Halldin,
375 2002; Roulet, 1991). By accounting for the elevational changes in the [ground surface of the surrounding](#)
376 [mire \(and thus not open water\), we ensure that the presented height values reflect height of the palsa](#)
377 [mounds and thus hold true to the morphological definition of palsas.](#) ~~surrounding the palsas, we have~~
378 ~~corrected for this effect.~~ [Since palsa mires are very dynamic landscapes, each correction brings](#)
379 [uncertainties.](#) ~~Though,~~ [The closely aligned elevation profiles \(Fig. 7\) give us confidence that the presented](#)
380 [height changes are primarily a result of freeze-thaw dynamics of the palsas.](#)

381 ~~We present seasonal patterns at a high spatial resolution over the full spatial extent of two large palsas.~~
382 While other studies have applied multitemporal LiDAR for detecting permafrost dynamics, they have ~~been~~
383 [used](#) terrestrial LiDAR scanning (Anders et al., 2020) rather than UAV-borne LiDAR, or else inter-annual
384 airborne LiDAR (e.g. Douglas et al., 2021; Jones et al., 2015), [which generally has meter-scale spatial](#)
385 [resolutions and infrequent revisit turn periods.](#) Anders et al., (2020) performed three TLS measurements
386 over 14 months (June 2015, Aug ~~2015~~2015, and Aug 2016) to observe thaw subsidence of a permafrost
387 area in Northwest Territories, Canada, finding a total change of 1.4 cm; they determined that the TLS
388 measurements were more accurate than those from field-based surveying. [While promising, the mobility](#)
389 [and range of UAV LiDAR is particularly advantageous when surveying permafrost features in peat- or](#)
390 [wetland landscapes.](#)

391 ~~Another approach to quantify~~ [longer-term subsidence and](#) the effect of seasonal freeze/thaw dynamics ~~on~~
392 [topography](#) ~~is~~ through the use of InSAR remote sensing (de la Barreda-Bautista et al., 2022; Kou et al.,
393 2021; Valman et al., 2024; Yanagiya et al., 2023), [which can be an effective method to detect the signal of](#)
394 [subsidence.](#) [de la Barreda-Bautista et al. \(2022\) reported a maximum subsidence rate of 1.5 cm, from](#)
395 [InSAR data, between 2017 and 2020 on a palsa plateau at ca. 100 km from the Vissátvuopmi palsa](#)
396 [complex.](#) Due to ~~its~~ ~~the~~ ~~coarser~~ ~~spatial resolution~~ ~~grid cell size (20 m) of the resulting data,~~ ~~however,~~ it is
397 likely to underestimate actual heave and subsidence values of smaller isolated features such as palsas.

398 [Over the same period and location, they observed 25 cm subsidence from DEMs created with UAV](#)
399 [photogrammetry. InSAR subsidence has also been analyzed at the Vissátvuopmi palsa complex](#) (Valman
400 [et al., 2024\). They found that Vissátvuopmi and the adjacent Árbuvuopmi are the fastest subsiding](#)
401 [complexes of the eight studied in northern Sweden, with maximum subsidence rates of -8.9 and -9.9 mm](#)
402 [yr⁻¹ between 2017 and 2021. While the absolute values are not comparable with subsidence rates from our](#)
403 [UAV LiDAR data, possibly due to the larger ~~discrepancy in spatial resolution~~ grid cell size from InSAR](#)
404 [analysis, they give an important context of the subsidence trend across the entire palsa complex in the](#)
405 [years right before our study period. The fact that Vissátvuopmi is among the most quickly deforming](#)
406 [complexes and at the same time does not hold a protected status, emphasizes the importance of studies](#)
407 [conducted here.](#)

408 [In our study, we show that the elevation change of the Dome palsa ~~in~~ as a whole from September 2022 to](#)
409 [September 2023 was minor and mostly within the 0.030 m error range, while the Ridge palsa did subside](#)
410 [on average 0.07 m within one year. A ~~h~~ hypothesis for this is related to the surrounding thermokarst ponds.](#)
411 [The Ridge palsa is surrounded by relatively larger and deeper thermokarst ponds, which could enhance](#)
412 [vertical subsidence more centrally in the palsas as a result of increased heat transfer to the palsa core. To](#)
413 [find out if the higher subsidence on this palsa is a robust signal and what processes are responsible for](#)
414 [this, continued annual LiDAR surveys and observations of the palsa's interior via geophysical imaging are](#)
415 [needed.](#)

416 [5.2 Lateral palsa degradation](#)

417 The time series from this study showed not only the seasonal heave and subsidence patterns, but also
418 revealed a ~~large area of~~ degradation [hotspot](#) on ~~one of the~~ [Dome](#) palsas that happened between September
419 2022 and April 2023. By comparing the elevation profiles ~~at~~ [and histograms of change between for](#) these
420 two timestamps [in the northwest part of the Dome palsa at the degradation hotspot](#) (Fig. 7e [and Fig. 6i](#)), we
421 can see that a drop of up to 0.4 m happened within the autumn and/or winter season, despite the presence
422 of a snow cover in April. It is important to consider that positive air temperatures persisted until the end of
423 October 2022 (Fig. 2), which suggests that the subsidence likely ~~—~~ continued into the late autumn [2022](#)

424 period, influenced by prolonged thawing conditions. Whether this entire drop in palsa height occurred solely
425 between the September 2022 campaign and the freeze-up of the entire active layer, or if gravitational
426 processes also contributed after the complete freeze-up, remains uncertain. Regarding the initiation of the
427 degradation at this location, it is likely that it was ongoing earlier in the summer of 2022. Both the air
428 temperatures ($>20\text{ }^{\circ}\text{C}$) and precipitation (158 mm) (both measured at Saarikoski weather station) peaked
429 in July of that year, which could have resulted in a deeply thawed, saturated upper layer of the palsa and
430 initiated a progressive lateral degradation event. Additionally, the precipitation in this winter was greater
431 than the previous winter, which may have caused additional warming of the ground, either via a thicker
432 snowpack (F-Zhang, 2005) or latent heat brought by rainfall (Putkonen & Roe, 2003). This falls in line with
433 Olvmo et al. (2020), who conclude that increased winter precipitation is one of the main causes of rapid
434 palsa degradation in the study region.

435 -The characteristic of this ~~lateral degradation~~ degradation hotspot is similar to that described in Martin et al.
436 (2021) as “constant edge degradation”, which they found as the second phase of lateral degradation on
437 peat plateaus following “initial slope adjustment” and preceding “plateau collapse” phases. While both the
438 spatial and temporal scale differ between their and our study, this could indicate that a more widespread
439 collapse or subsidence can follow on the Dome palsa. As described in (Valman et al., (2024), approaches
440 that identify initial signs of permafrost degradation with the use of repeated measurements are needed, to
441 which our study adds. In order to make more conclusive statements about the reason for this rapid
442 degradation, the monitoring of ground temperatures and knowledge of the internal structure of this palsa is
443 required.

444 ~~While this~~ The described degradation hotspot could be just an isolated event, or a precursor to rapid
445 degradation in the following years.

446 ~~the elevation change of the Dome palsa as a whole from September 2022 to September 2023 was minor.~~
447 ~~The Ridge palsa, however, did subside on average 0.07 m within one year. The faster degradation on this~~
448 ~~specific palsa is in line with observations in~~ Olvmo et al. (2020) found an average annual decay rate (loss
449 of palsa area) of $-0.74\text{ }\%a^{-1}$ and $-2.45\text{ }\%a^{-1}$ ~~betweenfor respectively~~ the Dome and Ridge palsas
450 respectively, for the period 2010–2016. Using the palsa area from Olvmo et al. (2020) in 2016 and the

451 [extent in 2023 from our study, we can calculate a new annual decay rate. For the period 2016–2023, we](#)
452 [found respective rates of -3.27 %a⁻¹ and -1.55 %a⁻¹. The -2.53 %a⁻¹ change in decay rate on the Dome](#)
453 [palsa can be largely explained by the degradation hotspot, which covered ca. 2.6% of the total palsa area.](#)
454 [The slight decrease in annual decay rate on the Ridge palsa could be explained by a stabilization of](#)
455 [degraded areas. When excluding the degradation hotspot on the Dome palsa, the Ridge palsa lost a larger](#)
456 [percentage of its extent, similar to Olvmo et al. \(2020\). Again, lateral water fluxes greatly affect ground](#)
457 [temperatures and permafrost degradation \(Martin et al., 2021; Sjöberg et al., 2016; Walvoord & Kurylyk,](#)
458 [2016\). Therefore, smaller palsas are relatively more susceptible to lateral erosion through heat and water](#)
459 [fluxes, provided by surrounding thermokarst ponds, compared to larger palsas \(e.g. Borge et al., 2017\).](#)
460 ~~[\(Martin et al., 2021; Sjöberg et al., 2016; Walvoord & Kurylyk, 2016\)](#)~~

461 **5.3.2 Using UAV LiDAR to monitor permafrost landscapes**

462 The use of UAVs in assessing permafrost landscapes has increased in recent years ([e.g. de la Barreda-](#)
463 [Bautista et al., 2022; Krutskikh et al., 2023; Martin et al., 2021; Siewert & Olofsson, 2020; Sjögersten et al.,](#)
464 [2023; Verdonen et al., 2023](#)), although primarily with the use of photogrammetry. Changes in the exterior
465 of permafrost peatlands can be subtle and therefore require the use of highly accurate methods [of](#)
466 [measuring ground elevation](#), particularly for vertical subsidence, and when studied over relatively short
467 timescales.

468 A challenge in permafrost environments, especially palsa mires, is the lack of stable elevation points to be
469 used for ground control points (GCPs). In this study, GCPs were not used, ~~however,~~ [all](#) point
470 clouds were obtained using GNSS, post-processed as described in 3.2, and visually checked [over the](#)
471 [whole scanned area](#) for consistency. The elevation profiles (Fig. 7) from the five campaigns are well-aligned
472 and thereby confirm that the positional data are highly accurate. As mentioned by Harder (2020), the use
473 of GCPs is not strictly necessary for UAV LiDAR applications, which significantly contributes to the efficient
474 field visits in harsh Arctic conditions.

475 In this study, we employed the YellowScan Mapper (YSM) system in September 2022 and the YellowScan
476 Mapper_+ (YSM+) in the four campaigns in 2023. The use of an upgraded LiDAR system after the first

477 scanning introduces a potential source of uncertainty in our measurements. However, both systems
478 achieved high point densities (>1,000 points/m²), ensuring detailed surface representation in both datasets
479 despite the difference in the number of recorded returns per pulse. Furthermore, the alignment and
480 positioning of the data were visually verified, showing that the impact of using different systems on our
481 results is minimal. The vertical accuracy of the YSM and YSM+ systems used here have an RMSE of 2.8
482 and 2.1 cm, respectively. This is a potential error source in the data and changes less than ~~these~~
483 propagated error (See Fig. 6a–h) are within the margin of error. The main findings of the study, which
484 include the observed 0.15 m mean heave in winter and associated subsidence over summer and the
485 identification of a degradation hotspot, are larger than the described error.— Both YellowScan LiDAR
486 systems have a minimum distance of 1 m between registered returns at a flying height of 60 m. This means
487 that all objects on the surface shorter than 1 m in height will be measured by a single return. In this case,
488 to measure the ground elevation underneath vegetation cover requires high point density, which was
489 acquired in this study. By using the minimum elevation per grid cell, the resulting DTM should exclude
490 vegetation heights. In our study, the diffuse cover of *Betula nana* ranged from 0-100% per m² over both
491 palsas, yet the ground could almost always be seen between the sparse branches. Careful consideration
492 of acquisition parameters and algorithms is needed when UAV LiDAR ~~is~~ to be used to create DTMs in
493 areas of extremely dense vegetation cover, or when small grid cell sizes are needed to allow determination
494 of the ground elevation (Kucharczyk et al., 2018).

495 The ability of LiDAR instruments to measure ground elevation below the vegetation canopy is one of the
496 major advantages that LiDAR has over photogrammetry. Fig. 3 shows, for example, the Ridge palsa with
497 several large birch trees, where terrain analysis can still be done below the canopy. Photogrammetry
498 creates surface models that consist of vegetation height, which is likely to increase over the vegetation
499 season, adding bias to the models. The observed frost heave and subsidence in our study would not have
500 been soundly established with just the use of ~~photogrammetrically-derived surface models or the photos or~~
501 ~~aerial imagery~~, due to the potential confusion between vegetation and ground height. A disadvantage when
502 comparing LiDAR and photogrammetric methods is the higher costs of UAV LiDAR scanners at the present
503 time. For that reason alone, when one's objective is to merely compare the perimeter of palsas (e.g, lateral
504 degradation) or other landforms with low-growing vegetation, photogrammetry might still be preferred. While

505 some UAV LiDAR systems can also be integrated with an RGB camera, due to the additional costs, this
506 was not done in this study. The main advantage that this would give is an improved visualization through
507 use of colorized point clouds and could thereby improve the delineation of, for example, snow-covered (or
508 -free) areas.

509 UAVs present several advantages over 'classic' airborne LiDAR surveys, including higher spatial resolution
510 DTMs, simpler planning, and reduced costs, particularly for smaller spatial extents. Additionally, the
511 increased temporal frequency achievable with UAVs enables more frequent data acquisition, which is
512 essential for monitoring intra-annual dynamics in permafrost landscapes.~~When compared to 'classic'~~
513 ~~airborne LiDAR surveys, the potential for higher spatial resolution DTMs, ease of planning and lower~~
514 ~~associated costs do largely favor the use of a UAV when studying permafrost landscapes at least over~~
515 ~~smaller spatial extents.~~

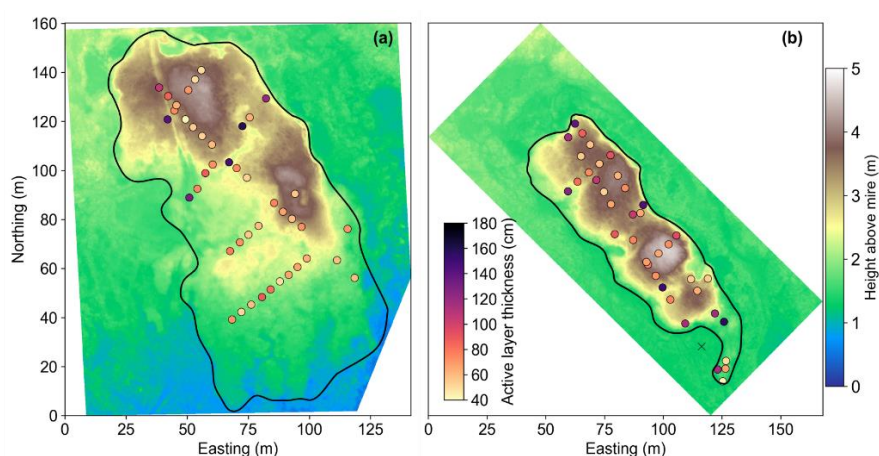
516 **6 Conclusions**

517 This study has provided insights into the intra-annual dynamics of palsas through the use of repeat UAV
518 LiDAR measurements, which we highlight as an effective tool for detailed change detection in permafrost
519 landscapes. We present a unique time series of five UAV LiDAR campaigns during a one-year time span
520 on two large palsas in Sweden's largest coherent palsa mire complex. The study revealed seasonal
521 variations in the palsa's topography, with an average frost heave and thaw subsidence of 0.15 m (and up
522 to 0.30 m), with the highest rate of subsidence on the palsas between June and July. The time series also
523 shows a considerable lateral degradation hotspot in a 300-225 m² section ~~at~~of one of the palsas, with a
524 subsidence of up to 0.5-1.92-0 m over the one-year study period. This substantial permafrost degradation
525 occurred between September 2022 and April 2023 which suggests that the degradation of palsas is not
526 limited to the summer months. To conclude, the use of repeat UAV LiDAR scanning has proven to be a
527 highly effective tool for capturing detailed seasonal measurements of permafrost dynamics, which would
528 not have been observed if only annual measurements had been taken.

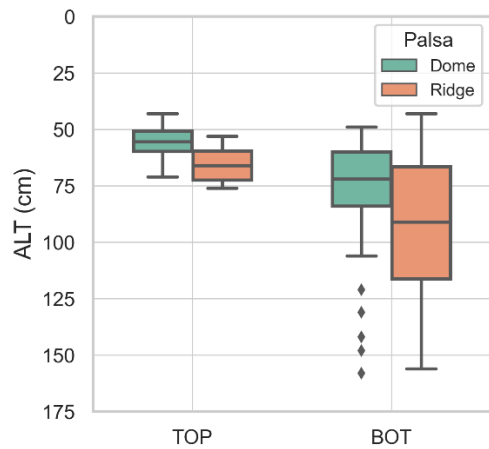
529

530 **Appendix A: Active layer thickness**

531 The thickness of the active layer (ALT) is measured in September 2023 at both the Dome and the Ridge
532 palsas by inserting a 1.80 m steel rod until the top of the frozen ground was **observed**met. The points (Fig.
533 A1) are either within the polygons of the parts that were snow-free in April 2023 (see Figs. 6a, b, d and e)
534 or in a lower part of the palsa. The former points are assigned 'TOP', while the latter are assigned 'BOT'.
535 The points in the 'TOP' class have a thinner and more narrowly spread ALT compared to the points in the
536 'BOT' class (Fig. A2).



537 **Figure A1. Active layer thickness (ALT) on the Dome palsa (a) and Ridge palsa (b) in September 2023 with their**
538 **corresponding DTMs.**



540 **Figure A2. Distribution of the ALT at both palsas, showing that ALT in the top-positions is generally lower and**
541 **more narrowly spread compared to the points in the lower parts or depressions.**

544 **Data availability**

545 The data presented in this article are stored at <https://zenodo.org/records/104970940.5281/zenodo.10497093> (Renette., 2024).

547 **Author contribution**

548 CR and HR designed the study and performed the UAV surveys. HR acquired funding. CR handled data
549 processing, analysis, and figure creation. ST and BH assisted in the setup of the weather station. MO and
550 BH contributed expertise and advice. The manuscript was initially prepared by CR, assisted by HR. All
551 authors reviewed and edited the manuscript draft. All authors approved the final version for submission.

552 **Competing interests**

553 The authors declare that they have no conflict of interest.

554 **Acknowledgements**

555 This work was supported by the Swedish Research Council Formas (grant number 2022-00959),
556 “Threatened subarctic palsa mires: a new integrated approach to map and understand permafrost
557 degradation”. Also, we thank all those that helped with fieldwork and logistics. [Finally, we would like to
558 thank reviewers Jan Henrik Blöthe and Martha Ledger for their valuable comments and suggestions, which
559 significantly improved the quality of the manuscript.](#)

560

561

562 **References**

- 563 Anders, K., Marx, S., Boike, J., Herfort, B., Wilcox, E. J., Langer, M., Marsh, P., & Höfle, B. (2020).
564 Multitemporal terrestrial laser scanning point clouds for thaw subsidence observation at Arctic
565 permafrost monitoring sites. *Earth Surface Processes and Landforms*, *45*(7), 1589–1600.
566 <https://doi.org/10.1002/esp.4833>
- 567 Andersson, L., Rafstedt, T., & von Sydow, U. (1985). *FJALLENS VEGETATION Norrbottens län: En*
568 *översikt av Norrbottenfjällens vegetation baserad på vegetationskartering och naturvärdering*.
569 Naturvårdsverket. <https://urn.kb.se/resolve?urn=urn:nbn:se:naturvardsverket:diva-7479>
- 570 Backe, S. (2014). *Kartering av Sveriges palsmyrar* (pp. 1–54) [Text].
571 [https://www.lansstyrelsen.se/norrboten/om-oss/vara-tjanster/publikationer/2014/kartering-av-](https://www.lansstyrelsen.se/norrboten/om-oss/vara-tjanster/publikationer/2014/kartering-av-sveriges-palsmyrar.html)
572 [sveriges-palsmyrar.html](https://www.lansstyrelsen.se/norrboten/om-oss/vara-tjanster/publikationer/2014/kartering-av-sveriges-palsmyrar.html)
- 573 Biskaborn, B. K., Smith, S. L., Noetzli, J., Matthes, H., Vieira, G., Streletskiy, D. A., Schoeneich, P.,
574 Romanovsky, V. E., Lewkowitz, A. G., Abramov, A., Allard, M., Boike, J., Cable, W. L.,
575 Christiansen, H. H., Delaloye, R., Diekmann, B., Drozdov, D., Etzelmüller, B., Grosse, G., ...
576 Lantuit, H. (2019). Permafrost is warming at a global scale. *Nature Communications*, *10*(1),
577 Article 1. <https://doi.org/10.1038/s41467-018-08240-4>
- 578 Borge, A. F., Westermann, S., Solheim, I., & Etzelmüller, B. (2017). Strong degradation of palsas and
579 peat plateaus in northern Norway during the last 60 years. *The Cryosphere*, *11*(1), 1–16.
580 <https://doi.org/10.5194/tc-11-1-2017>
- 581 *CloudCompare* (2.12.4). (2023). [Computer software]. GPL software.
582 <https://www.danielgm.net/cc/release/>
- 583 *CloudStation* (2309.0.0). (2023). [Computer software]. YellowScan.
584 <https://www.yellowscan.com/products/cloudstation/>
- 585 Curcio, A. C., Peralta, G., Aranda, M., & Barbero, L. (2022). Evaluating the Performance of High Spatial
586 Resolution UAV-Photogrammetry and UAV-LiDAR for Salt Marshes: The Cádiz Bay Study Case.
587 *Remote Sensing*, *14*(15), Article 15. <https://doi.org/10.3390/rs14153582>
- 588 de la Barrera-Bautista, B., Boyd, D. S., Ledger, M., Siewert, M. B., Chandler, C., Bradley, A. V., Gee, D.,
589 Large, D. J., Olofsson, J., Sowter, A., & Sjögersten, S. (2022). Towards a Monitoring Approach

590 for Understanding Permafrost Degradation and Linked Subsidence in Arctic Peatlands. *Remote*
591 *Sensing*, 14(3), Article 3. <https://doi.org/10.3390/rs14030444>

592 Douglas, T. A., Hiemstra, C. A., Anderson, J. E., Barbato, R. A., Bjella, K. L., Deeb, E. J., Gelvin, A. B.,
593 Nelsen, P. E., Newman, S. D., Saari, S. P., & Wagner, A. M. (2021). Recent degradation of
594 interior Alaska permafrost mapped with ground surveys, geophysics, deep drilling, and repeat
595 airborne lidar. *The Cryosphere*, 15(8), 3555–3575. <https://doi.org/10.5194/tc-15-3555-2021>

596 [EUNIS - Factsheet for Palsa mires. \(2013\). Retrieved November 10, 2023, from](https://eunis.eea.europa.eu/habitats/10155)
597 <https://eunis.eea.europa.eu/habitats/10155>

598

599 Fewster, R. E., Morris, P. J., Ivanovic, R. F., Swindles, G. T., Peregón, A. M., & Smith, C. J. (2022).
600 _____ Imminent loss of climate space for permafrost peatlands in Europe and Western Siberia. *Nature*
601 _____ *Climate Change*, 12(4), 373–379. <https://doi.org/10.1038/s41558-022-01296-7>

602 Fu, Z., Wu, Q., Zhang, W., He, H., & Wang, L. (2022). Water Migration and Segregated Ice Formation in
603 Frozen Ground: Current Advances and Future Perspectives. *Frontiers in Earth Science*, 10.
604 <https://www.frontiersin.org/articles/10.3389/feart.2022.826961>

605 Gruber, S. (2020). Ground subsidence and heave over permafrost: Hourly time series reveal interannual,
606 seasonal and shorter-term movement caused by freezing, thawing and water movement. *The*
607 *Cryosphere*, 14(4), 1437–1447. <https://doi.org/10.5194/tc-14-1437-2020>

608 Harder, P., Pomeroy, J. W., & Helgason, W. D. (2020). Improving sub-canopy snow depth mapping with
609 unmanned aerial vehicles: Lidar versus structure-from-motion techniques. *The Cryosphere*, 14(6),
610 1919–1935. <https://doi.org/10.5194/tc-14-1919-2020>

611 Harris, S., French, H., Heginbottom, J., Johnston, G., Ladanyi, B., Sego, D., & Everdingen, R. (1988).
612 *Glossary of Permafrost and Related Ground-Ice Terms*. <https://doi.org/10.4224/20386561>

613 Hu, Y., Wang, J., Li, Z., & Peng, J. (2022). Ground surface elevation changes over permafrost areas
614 revealed by multiple GNSS interferometric reflectometry. *Journal of Geodesy*, 96(8), 56.
615 <https://doi.org/10.1007/s00190-022-01646-5>

616 Hugelius, G., Loisel, J., Chadburn, S., Jackson, R. B., Jones, M., MacDonald, G., Marushchak, M.,
617 Olefeldt, D., Packalen, M., Siewert, M. B., Treat, C., Turetsky, M., Voigt, C., & Yu, Z. (2020).
618 Large stocks of peatland carbon and nitrogen are vulnerable to permafrost thaw. *Proceedings of*
619 *the National Academy of Sciences*, *117*(34), 20438–20446.
620 <https://doi.org/10.1073/pnas.1916387117>

621 Iwahana, G., Busey, R. C., & Saito, K. (2021). Seasonal and Interannual Ground-Surface Displacement in
622 Intact and Disturbed Tundra along the Dalton Highway on the North Slope, Alaska. *Land*, *10*(1),
623 Article 1. <https://doi.org/10.3390/land10010022>

624 Jacobs, J. M., Hunsaker, A. G., Sullivan, F. B., Palace, M., Burakowski, E. A., Herrick, C., & Cho, E.
625 (2021). Snow depth mapping with unpiloted aerial system lidar observations: A case study in
626 Durham, New Hampshire, United States. *The Cryosphere*, *15*(3), 1485–1500.
627 <https://doi.org/10.5194/tc-15-1485-2021>

628 Jones, B. M., Grosse, G., Arp, C. D., Miller, E., Liu, L., Hayes, D. J., & Larsen, C. F. (2015). Recent Arctic
629 tundra fire initiates widespread thermokarst development. *Scientific Reports*, *5*(1), Article 1.
630 <https://doi.org/10.1038/srep15865>

631 Kellner, E., & Halldin, S. (2002). Water budget and surface-layer water storage in a Sphagnum bog in
632 central Sweden. *Hydrological Processes*, *16*(1), 87–103. <https://doi.org/10.1002/hyp.286>

633 Kou, X., Liu, X., Zhang, Y., Zhang, Y., Wang, T., & Yan, S. (2021). A Study on the Detection of
634 Deformation of Tuotuohe Area on the Qinghai-Tibet Plateau. *2021 IEEE International Geoscience*
635 *and Remote Sensing Symposium IGARSS*, 5362–5365.
636 <https://doi.org/10.1109/IGARSS47720.2021.9555061>

637 Krutskikh, N., Ryazantsev, P., Ignashov, P., & Kabonen, A. (2023). The Spatial Analysis of Vegetation
638 Cover and Permafrost Degradation for a Subarctic Palsa Mire Based on UAS Photogrammetry
639 and GPR Data in the Kola Peninsula. *Remote Sensing*, *15*, 1896.
640 <https://doi.org/10.3390/rs15071896>

641 Kucharczyk, M., Hugenholtz, C. H., & Zou, X. (2018). UAV–LiDAR accuracy in vegetated terrain. *Journal*
642 *of Unmanned Vehicle Systems*, *6*(4), 212–234. <https://doi.org/10.1139/juvs-2017-0030>

643 [Lantmateriet. 2021. GSD-Orthophoto. Available from https://www.lantmateriet.se/sv/Kartor-och-](https://www.lantmateriet.se/sv/Kartor-och-geografisk-information/geodataprodukter/produktlista/ortofoto/)
644 [geografisk-information/geodataprodukter/produktlista/ortofoto/](https://www.lantmateriet.se/sv/Kartor-och-geografisk-information/geodataprodukter/produktlista/ortofoto/) [accessed 1 Nov 2023].

645 Łakomiec, P., Holst, J., Friborg, T., Crill, P., Rakos, N., Kljun, N., Olsson, P.-O., Eklundh, L., Persson, A.,
646 & Rinne, J. (2021). Field-scale CH₄ emission at a subarctic mire with heterogeneous permafrost
647 thaw status. *Biogeosciences*, 18(20), 5811–5830. <https://doi.org/10.5194/bg-18-5811-2021>

648 Lin, Y.-C., Cheng, Y.-T., Zhou, T., Ravi, R., Hasheminasab, S. M., Flatt, J. E., Troy, C., & Habib, A.
649 (2019). Evaluation of UAV LiDAR for Mapping Coastal Environments. *Remote Sensing*, 11(24),
650 Article 24. <https://doi.org/10.3390/rs11242893>

651 Luoto, M., Fronzek, S., & Zuidhoff, F. S. (2004a). Spatial modelling of palsa mires in relation to climate in
652 northern Europe. *Earth Surface Processes and Landforms*, 29(11), 1373–1387.
653 <https://doi.org/10.1002/esp.1099>

654 Luoto, M., Heikkinen, R. K., & Carter, T. R. (2004b). Loss of palsa mires in Europe and biological
655 consequences. *Environmental Conservation*, 31(1), 30–37.
656 <https://doi.org/10.1017/S0376892904001018>

657 Mamet, S. D., Chun, K. P., Kershaw, G. G. L., Loranty, M. M., & Peter Kershaw, G. (2017). Recent
658 Increases in Permafrost Thaw Rates and Areal Loss of Palsas in the Western Northwest
659 Territories, Canada: Non-linear Palsa Degradation. *Permafrost and Periglacial Processes*, 28(4),
660 619–633. <https://doi.org/10.1002/ppp.1951>

661 Martin, L. C. P., Nitzbon, J., Scheer, J., Aas, K. S., Eiken, T., Langer, M., Filhol, S., Eitzelmüller, B., &
662 Westermann, S. (2021). Lateral thermokarst patterns in permafrost peat plateaus in northern
663 Norway. *The Cryosphere*, 15(7), 3423–3442. <https://doi.org/10.5194/tc-15-3423-2021>

664 Olvmo, M., Holmer, B., Thorsson, S., Reese, H., & Lindberg, F. (2020). Sub-arctic palsa degradation and
665 the role of climatic drivers in the largest coherent palsa mire complex in Sweden (Vissátvuopmi),
666 1955–2016. *Scientific Reports*, 10(1), Article 1. <https://doi.org/10.1038/s41598-020-65719-1>

667 Ostrowski, W., Górski, K., Pilarska, M., Salach, A., & Bakula, K. (2017). Comparison of the laser scanning
668 solutions for the unmanned aerial vehicles. *Archiwum Fotogrametrii, Kartografii i Teledetekcji*, 29,
669 101–123. <https://doi.org/10.14681/afkit.2017.008>

670 Pirk, N., Aalstad, K., Mannerfelt, E. S., Clayer, F., de Wit, H., Christiansen, C. T., Althuizen, I., Lee, H., &
671 Westermann, S. (2024). Disaggregating the Carbon Exchange of Degrading Permafrost
672 Peatlands Using Bayesian Deep Learning. *Geophysical Research Letters*, 51(10),
673 e2024GL109283. <https://doi.org/10.1029/2024GL109283>

674 [POSPac UAV \(8.2\). \(2023\). \[Computer software\]. Applanix. https://www.applanix.com/products/pospac-](https://www.applanix.com/products/pospac-uav.html)
675 [uav.html](https://www.applanix.com/products/pospac-uav.html)

676 ~~[POSPac UAV \(8.2\). \(2023\). \[Computer software\]. Applanix. https://www.applanix.com/products/pospac-](https://www.applanix.com/products/pospac-uav.htm)~~
677 ~~[uav.htm](https://www.applanix.com/products/pospac-uav.htm)~~

678 Putkonen, J., & Roe, G. (2003). Rain-on-snow events impact soil temperatures and affect ungulate
679 survival. *Geophysical Research Letters - GEOPHYS RES LETT*, 30, 37–1.
680 <https://doi.org/10.1029/2002GL016326>

681 [Renette, C. \(2024\). Dataset for: "Multitemporal UAV LiDAR detects seasonal heave and subsidence on](#)
682 [palsas" \(Renette et al., 2024\) V1.0, Zenodo \[data set\], 10.5281/zenodo.10497094](#)

683 [Romanovsky, V. E., & Osterkamp, T. E. \(1995\). Interannual variations of the thermal regime of the active](#)
684 [layer and near-surface permafrost in northern Alaska. *Permafrost and Periglacial Processes*,](#)
685 [6\(4\), 313–335. https://doi.org/10.1002/ppp.3430060404](#)

686 [Roulet, N. T. \(1991\). Surface Level and Water Table Fluctuations in a Subarctic Fen. *Arctic and Alpine*](#)
687 [Research, 23\(3\), 303–310. https://doi.org/10.2307/1551608](#)

688 [Seppälä, M. \(1986\). The Origin of Palsas. *Geografiska Annaler: Series A, Physical Geography*, 68\(3\),](#)
689 [141–147. https://doi.org/10.1080/04353676.1986.11880167](#)

690 [Siewert, M. B., & Olofsson, J. \(2020\). Scale-dependency of Arctic ecosystem properties revealed by UAV.](#)
691 [Environmental Research Letters, 15\(9\), 094030. https://doi.org/10.1088/1748-9326/aba20b](#)

692 [Sjöberg, Y., Coon, E., K. Sannel, A. B., Pannetier, R., Harp, D., Frampton, A., Painter, S. L., & Lyon, S.](#)
693 [W. \(2016\). Thermal effects of groundwater flow through subarctic fens: A case study based on](#)
694 [field observations and numerical modeling. *Water Resources Research*, 52\(3\), 1591–1606.](#)
695 <https://doi.org/10.1002/2015WR017571>

696 [Sjögersten, S., Ledger, M., Siewert, M., De la Barreda-Bautista, B., Sowter, A., Gee, D., Foody, G., &](#)
697 [Boyd, D. \(2023\). Optical and radar Earth observation data for upscaling methane emissions](#)

698 [linked to permafrost degradation in sub-Arctic peatlands in northern Sweden. *Biogeosciences*, 20,](#)
699 [4221–4239. https://doi.org/10.5194/bg-20-4221-2023](#)

700 [Smith, S. L., O'Neill, H. B., Isaksen, K., Noetzli, J., & Romanovsky, V. E. \(2022\). The changing thermal](#)
701 [state of permafrost. *Nature Reviews Earth & Environment*, 3\(1\), Article 1.](#)
702 [https://doi.org/10.1038/s43017-021-00240-1](#)

703 [Swindles, G. T., Morris, P. J., Mullan, D., Watson, E. J., Turner, T. E., Roland, T. P., Amesbury, M. J.,](#)
704 [Kokfelt, U., Schoning, K., Pratte, S., Gallego-Sala, A., Charman, D. J., Sanderson, N., Garneau,](#)
705 [M., Carrivick, J. L., Woulds, C., Holden, J., Parry, L., & Galloway, J. M. \(2015\). The long-term fate](#)
706 [of permafrost peatlands under rapid climate warming. *Scientific Reports*, 5\(1\), Article 1.](#)
707 [https://doi.org/10.1038/srep17951](#)

708 [Taylor, J. R. \(1997\). Introduction to Error Analysis, the Study of Uncertainties in Physical Measurements](#)
709 [\(2nd ed.\). *University Science Books*, ISBN 093570275X.](#)

710 [Valman, S., Siewert, M. B., Boyd, D., Ledger, M., Gee, D., de la Barreda-Bautista, B., Sowter, A., &](#)
711 [Sjögersten, S. \(2024\). InSAR-measured permafrost degradation of palsa peatlands in northern](#)
712 [Sweden. *The Cryosphere*, 18\(4\), 1773–1790. https://doi.org/10.5194/tc-18-1773-2024](#)

713 [Verdonen, M., Störmer, A., Lotsari, E., Korpelainen, P., Burkhard, B., Colpaert, A., & Kumpula, T. \(2023\).](#)
714 [Permafrost degradation at two monitored palsa mires in north-west Finland. *The Cryosphere*,](#)
715 [17\(5\), 1803–1819. https://doi.org/10.5194/tc-17-1803-2023](#)

716 [Voigt, C., Marushchak, M. E., Mastepanov, M., Lamprecht, R. E., Christensen, T. R., Dorodnikov, M.,](#)
717 [Jackowicz-Korczyński, M., Lindgren, A., Lohila, A., Nykänen, H., Oinonen, M., Oksanen, T.,](#)
718 [Palonen, V., Treat, C. C., Martikainen, P. J., & Biasi, C. \(2019\). Ecosystem carbon response of](#)
719 [an Arctic peatland to simulated permafrost thaw. *Global Change Biology*, 25\(5\), 1746–1764.](#)
720 [https://doi.org/10.1111/gcb.14574](#)

721 [Walvoord, M. A., & Kurylyk, B. L. \(2016\). Hydraulic impacts of permafrost thawing and implications for](#)
722 [groundwater fluxes in the Arctic. *Water Resources Research*, 52\(2\), 1236–1255.](#)
723 [https://doi.org/10.1002/2015WR018299](#)

724 [Yanagiya, K., Furuya, M., Danilov, P., & Iwahana, G. \(2023\). Transient Freeze-Thaw Deformation](#)
725 [Responses to the 2018 and 2019 Fires Near Batagaika Megaslump, Northeast Siberia. *Journal of*](#)
726 [Geophysical Research: Earth Surface, 128. <https://doi.org/10.1029/2022JF006817>](#)

727 [Zhang, T. \(2005\). Influence of the seasonal snow cover on the ground thermal regime: An overview.](#)
728 [Reviews of Geophysics - REV GEOPHYS, 43. <https://doi.org/10.1029/2004RG000157>](#)

729 [Zhang, W., Qi, J., Wan, P., Wang, H., Xie, D., Wang, X., & Yan, G. \(2016\). An Easy-to-Use Airborne](#)
730 [LiDAR Data Filtering Method Based on Cloth Simulation. *Remote Sensing*, 8\(6\), Article 6.](#)
731 <https://doi.org/10.3390/rs8060501>

732 [Zwieback, S., & Meyer, F. J. \(2021\). Top-of-permafrost ground ice indicated by remotely sensed late-](#)
733 [season subsidence. *The Cryosphere*, 15\(4\), 2041–2055. <https://doi.org/10.5194/tc-15-2041-2021>](#)

734

735 [Roulet, N. T. \(1991\). Surface Level and Water Table Fluctuations in a Subarctic Fen. *Arctic and Alpine*](#)
736 [Research, 23\(3\), 303–310. <https://doi.org/10.2307/1551608>](#)

737 [Seppälä, M. \(1986\). The Origin of Palsas. *Geografiska Annaler: Series A, Physical Geography*, 68\(3\),](#)
738 [141–147. <https://doi.org/10.1080/04353676.1986.11880167>](#)

739 [Siewert, M. B., & Olofsson, J. \(2020\). Scale-dependency of Arctic ecosystem properties revealed by UAV.](#)
740 [Environmental Research Letters, 15\(9\), 094030. <https://doi.org/10.1088/1748-9326/aba20b>](#)

741 [Sjögersten, S., Ledger, M., Siewert, M., De la Barrera-Bautista, B., Sowter, A., Gee, D., Foody, G., &](#)
742 [Boyd, D. \(2023\). Optical and radar Earth observation data for upscaling methane emissions](#)
743 [linked to permafrost degradation in sub-Arctic peatlands in northern Sweden. *Biogeosciences*, 20,](#)
744 [4221–4239. <https://doi.org/10.5194/bg-20-4221-2023>](#)

745 [Swindles, G. T., Morris, P. J., Mullan, D., Watson, E. J., Turner, T. E., Roland, T. P., Amesbury, M. J.,](#)
746 [Kokfelt, U., Schoning, K., Pratte, S., Gallego-Sala, A., Charman, D. J., Sanderson, N., Garneau, M.,](#)
747 [Carrivick, J. L., Woulds, C., Holden, J., Parry, L., & Galloway, J. M. \(2015\). The long-term fate of](#)
748 [permafrost peatlands under rapid climate warming. *Scientific Reports*, 5\(1\), Article 1.](#)
749 <https://doi.org/10.1038/srep17951>

750 Valman, S., Siewert, M. B., Boyd, D., Ledger, M., Gee, D., de la Barrera-Bautista, B., Sowter, A., &
751 Sjögersten, S. (2024). InSAR-measured permafrost degradation of palsas peatlands in northern
752 Sweden. *The Cryosphere*, 18(4), 1773–1790. <https://doi.org/10.5194/tc-18-1773-2024>

753 Verdonen, M., Störmer, A., Korpelainen, P., Lotsari, E., Burkhard, B., Colpaert, A., & Kumpula, T. (2022).
754 Permafrost degradation at two monitored palsas mires in north-west Finland. *EGU sphere*, 1–23.
755 <https://doi.org/10.5194/egusphere-2022-1173>

756 Verdonen, M., Störmer, A., Lotsari, E., Korpelainen, P., Burkhard, B., Colpaert, A., & Kumpula, T. (2023).
757 Permafrost degradation at two monitored palsas mires in north-west Finland. *The Cryosphere*, 17(5),
758 1803–1819. <https://doi.org/10.5194/tc-17-1803-2023>

759 Voigt, C., Marushchak, M. E., Mastepanov, M., Lamprecht, R. E., Christensen, T. R., Dorodnikov, M.,
760 Jackowicz-Korczyński, M., Lindgren, A., Lohila, A., Nykänen, H., Oinonen, M., Oksanen, T.,
761 Palonen, V., Treat, C. C., Martikainen, P. J., & Biasi, C. (2019). Ecosystem carbon response of
762 an Arctic peatland to simulated permafrost thaw. *Global Change Biology*, 25(5), 1746–1764.
763 <https://doi.org/10.1111/gcb.14574>

764 Yanagiya, K., Furuya, M., Danilov, P., & Iwahana, G. (2023). Transient Freeze-Thaw Deformation
765 Responses to the 2018 and 2019 Fires Near Batagaika Megaslump, Northeast Siberia. *Journal of*
766 *Geophysical Research: Earth Surface*, 128. <https://doi.org/10.1029/2022JF006817>

767 Zhang, T. (2005). Influence of the seasonal snow cover on the ground thermal regime: An overview.
768 *Reviews of Geophysics—REV GEOPHYS*, 43. <https://doi.org/10.1029/2004RG000157>

769 Zhang, W., Qi, J., Wan, P., Wang, H., Xie, D., Wang, X., & Yan, G. (2016). An Easy-to-Use Airborne
770 LiDAR Data Filtering Method Based on Cloth Simulation. *Remote Sensing*, 8(6), Article 6.
771 <https://doi.org/10.3390/rs8060501>

772 Zwieback, S., & Meyer, F. J. (2021). Top-of-permafrost ground ice indicated by remotely sensed late-
773 season subsidence. *The Cryosphere*, 15(4), 2041–2055. <https://doi.org/10.5194/tc-15-2041-2021>

774